AD-A091 629 STATE UNIV OF NEW YORK AT STONY BROOK DEPT OF MATERIA--ETC F/G 7/4
ION IMPLANTATION METALLURGY,(U)
MAR 79 C R CLAYTON, H HERMAN, S B AGARWAL N00014-77-C-0424
UNCLASSIFIED TR-1 NL

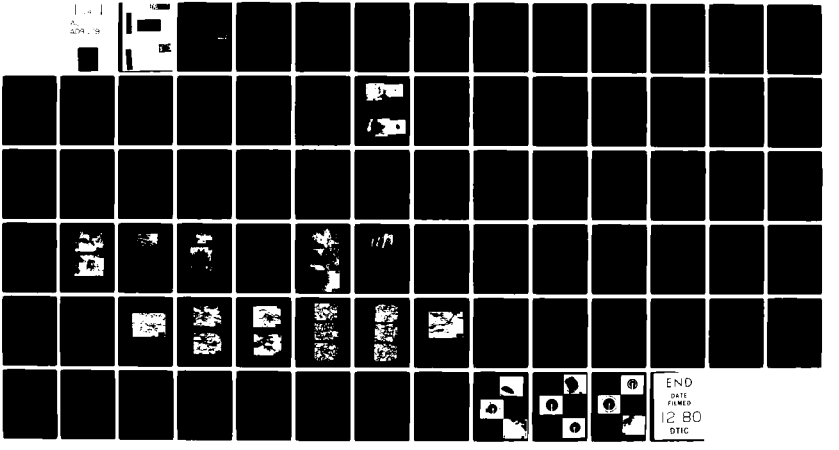

(6)

ION IMPLANTATION METALLURGY

(10) C.R. Clayton, H. Herman, S.B. Agarwal, N. Avadhany
K. Doss, W.-W. Hu and S. Prasad

(11) Mar[redacted]79

(14) TTR-1

AD91612

(9) Technical Report No. 1

to

The Office of Naval Research

Contract No. N00014-77-CO-424

(15) N00014-77-C-0424

Accession For	
NTIS GRA&I	☒
DDC TAB	☐
Unannounced	☐
Justification	
By	
Distribution/	
Availability Codes	
Dist.	Avail and/or special
A	

(12) 79

S/C 401014 GM

SYNOPSIS

The following studies have been carried out under this ONR-supported program:

. Modifications in the electrochemical and corrosion properties of 430 steel has been achieved by Ni-implantation. The work has revealed the following:

  (1) Anodic polarization behavior is in agreement with conventional alloying behavior.

  (2) Cathodic kinetic behavior, however, is not explained by conventional alloying theory, and would appear to be explained through the interaction of radiation induced defects and impurities.

  (3) That serious discrepancies exist between theoretical implantant distribution calculation and those observed by ESCA.

  (4) Evidence is found of marked segregation of solute Cr and implantant Ni, due to radiation enhanced diffusion.

. Improvements in the surface mechanical properties of 1018 steel are found to result from nitrogen implantation. We report on improvements in:

  (a) Fatigue-life

  (b) Cavitation-erosion resistance

  Supportive studies have included TEM analysis and Internal Friction studies.

. Metastable alloy studies have also been carried out on Be-Cu and Au-As systems.

INTERPRETATION OF ELECTROCHEMICAL BEHAVIOR OF NICKEL IMPLANTED TYPE 430 STAINLESS STEEL USING XPS AND TEM

INTRODUCTION

A number of electrochemical studies have been carried out on surface alloys which have been produced by ion implantation (1-6). For the most part these studies have been concerned with relatively low energy implantation (ca.25 KeV), yielding surface alloys in the depth range 50 - 150 Å. In an attempt to produce a surface alloy of more uniform composition with depth, extending to a level of at least 500 Å, we have carried out Ni-implantation into Type 430 ferritic stainless steel using a multi-implantation technique, at energies higher than are commonly used. We believe this level of implantation depth to be of technological significance as this is nearly two orders of magnitude thicker than most passive films. Reported here are results of structural, compositional and electrochemical analysis of the surface alloys formed.

EXPERIMENTAL

Commercial grade 430 stainless steel was annealed at 900°C for 10 hours and water quenched to eliminate sensitization. The samples were then polished to a 1 μm diamond paste finish. To eliminate extreme work hardening, the samples were vacuum annealed at 800°C for 1 hour and air cooled. They were then lightly polished with 1 μm diamond paste to remove surface segregants, leaving the surface only lightly cold worked. The samples were then ultrasonically cleaned with detergent solution and rinsed in distilled water.

The composition of the steel is given in Table 1.

A $^{58}Ni^{+}$ ion beam of 2.5 μA intensity was implanted into 1 cm^2 samples. The implantation parameters are given in Table 2. Three surface alloys were formed of surface composition approximating to 5, 15 and 30 At % Ni.

Composition of Surface Alloys

Calculated implantation profiles using LSS theory (7) corrected for sputtering have been compared in Figure 1 with composition depth profiles obtained with a VG ESCA 3 MK2 using Argon ion etching. It can be seen that the observed concentration of Nickel is higher in the surface regions than was predicted by LSS theory. In addition it was found that the Cr content of the steel was depleted within a region approximately 200 Å below the metal oxide interface. Beyond this region chromium enrichment, relative to the bulk alloy concentration, was observed. This is shown in figure 2.

TEM analysis of pre-thinned foils of 430, which were subsequently implanted with Ni, revealed considerable concentrations of point defects and dislocation entanglements. It can be seen from figure (3) that the level of radiation damage intensified with ion fluence and implantation energy. However, the SAD patterns revealed a nickel-rich BCC structure, indicating that elemental segregation did not lead to phase separation.

Figure (4) shows the relative abundance of Cr^{3+}, Fe^{3+} and Ni^{2+} in an oxide film formed on a freshly implanted sample. The plot was constructed from ESCA analysis of the Fe, Cr and Ni $2p^{3/2}$ peaks. Quantitative analysis was achieved by use of appropriate peak sensitivity factors (8). It appears that the relative concentrations of metals in the alloy and oxide layer are similar. Therefore, neither the surface alloy enrichment of Ni nor Cr depletion can be attributed to selective oxidation.

A more satisfactory explanation of the cause of elemental segregation has been postulated by Okamoto and Wiedersich (9). They have observed a similar segregational behavior of Ni and Cr in 316 stainless steel which was irradiated with 3.25 MeV Ni^+. They have suggested that the flow of radiation induced interstitials can cause flow of solute elements in different directions according to atomic misfit. Thus, undersized solute atoms such as Ni are thought to favor interstitial sites such as in the dumbbell configuration, whilst oversized solute atoms such as Cr diffuse away from sinks by vacancy migration.

ELECTROCHEMICAL ANALYSIS

Having defined the degree of surface modification by ion implantation from chemical and structural viewpoints, electrochemical analyses were carried out, aimed at studying the passivating properties of these modified 430 steel surfaces in aggressive aqueous environments. Of particular interest was the resistance of these surface alloys to pitting due to chloride attack.

POLARIZATION EXPERIMENTS

Samples were mounted in a teflon holder so that only the implanted surface would be exposed to the solution. The samples were washed in acetone and distilled water prior to emersion in the solution. To study the Active-Passive behavior hydrogen saturated 1N H_2SO_4 was used, prepared from reagent grade acid and double distilled water. The samples were always held at -900 mV(SCE) for 30 mins. to electrolytically reduce the oxide film. The anodic polarization sweep was carried out at a rate of 1 mV/sec.

For pitting studies anodic polarization at 1 mV/sec sweep rate was carried out in hydrogen saturated 1M NaCl solution. Again, the samples were cathodically pretreated at -900 mV to remove the oxide film.

DISCUSSION AND RESULTS

(a) Anodic Polarization in 1N H_2SO_4

The anodic polarization diagrams for the implanted and unimplanted samples are shown in figure (5) and the corresponding data are given in Table 3. Despite the surface depletion of Cr it would nevertheless appear that the overall shape of the polarization curves are influenced predominently by Cr. Nickel implantation has resulted in a marked reduction in the critical current density (Ic) for passivation, though having little or no influence upon the anodic slope in the active region. In the surface alloy of highest Ni content, a seven-fold reduction in critical current density was achieved, and pa ssive current density (Ip) was reduced by an order of magnitude. It would appear, therefore, that Ni-implantation improves the passivation properties of this steel in a very aggressive acid environment. However, the dominant effect that Cr has upon the passivity of this alloy is reflected in the small lowering of the passivation potential (Epp) and the constancy of the open circuit potential (E_{ocp}).

(b) Anodic Polarization in 1M NaCl Solution

Figure (6) shows the anodic polarization curves for the implanted and unimplanted steels. The samples were anodically polarized until the current density reached 10 $\mu A/cm^2$, whereupon the potential was reversed unti passivity was regained. The open circuit potentials $E_{(ocp)}$, the pitting potentials $E_{(pit)}$ and protection potentials $E_{(prot)}$ are given in Table 4.

The first significant alteration in the behavior of the 430 steel in 1M NaCl solution is seen to be the enoblement of the steel at open circuit potential. Implantation with Ni is also seen to significantly increase the resistance of the steel to pitting in chloride media. This is reflected in the increase in the positive value of the pitting potential. The surface alloy of highest Ni content again shows a strong influence upon the nature

of the passive film, as indicated by the value of the protection potential. The extent of this positive shift in the protection potential would indicate that the pits found in this case are of the order of the thickness of the alloy. It would be expected that little or no alteration would be expected from pits which are significantly deeper than the alloy thickness ($\sim$ 500 Å). However, the very pronounced effect of Cr enrichment found at deeper levels for this surface alloy may be responsible for pit growth arrest, leading to shallower pitting.

EFFECT OF Ni ON SECOND ANODIC CURRENT MAXIMA (SACM)

Factors Influencing the SACM of 430 Stainless Steel

The occurrence of the Second Anodic Current Maxima (SACM) during the anodic polarization of stainless steels has been reported in a number of studies (10-13). The second anodic maxima has been observed in polarization curves of steels of various structures and compositions. However, numerous different interpretations have been invoked to explain this characteristic of the anodic polarization curves. Some authors have proposed that the effect is associated with accelerated grain boundary dissolution due to the sensitization process which usually occurs in these alloys during the heat treatment cycle (12, 13). France and Greene (10) concluded that the SACM observed in 430 stainless steel was due to Ni enrichment on the surface during dissolution and showed Ni enrichment on the dissolved surface even in steels without any Ni. Kim and Wilde (11) showed anodic maxima to be due to oxidation of hydrogen which is a by-product of the cathodic reaction and could be absorbed into the alloy.

Fig. 5 shows that magnitude of second anodic maxima is dependent upon the level of Ni on the surface. The current at second anodic maxima goes down as Ni level is increased. On increasing the Ni concentration to 30% on the surface, the second anodic maxima is found to completely disappear though a break is observed at the potential where second anodic maxima is observed in 430 s.s. This shows that the presence of Ni is not responsible for the second anodic maxima as proposed by France and Greene. In fact, Ni suppresses the current maxima at 0.00 mV VsSCE.

It was shown by Kim and Wilde (11) that prolonged exposure to cathodic hydrogen evolution produces a passive current maxima, the amplitude of which

is related to the duration of the cathodic pretreatment. It was shown by Kim and Wilde, that even a steel which does not show second anodic maxima, if held at -800 mV for 30 min. would produce a second anodic maxima. However, 15 and 30% Ni implanted 430 s.s. did not show any second anodic maxima when held at -900 mV for 30 mins. To see the effect of exposure to cathodic exposure for longer periods, two implanted steels, which did not previously show second anodic maxima, were cathodically changed for 90 min. at -900 mV, and then anodically polarized. As shown in Fig. 7 & 8, in both steels, the maxima has emerged around 0.00 mV. Thus, as postulated by Kim and Wilde, the adsorbed hydrogen does oxidize at 0.00 mV, giving higher current density or anodic maxima. However, in their model, the current density due to hydrogen oxidation may be overestimated. It seems that hydrogen oxidation is not the only cause of second anodic maxima and there are other factors that contribute to current maxima in the passive range.

It is therefore concluded that in 430 stainless steel which had been held at 900°C for 10 hrs. followed by water quenching, some sensitization had occurred resulting in chromium depletion in grain boundary regions, and that the passive current emanating from these regions is higher than for the rest of the steel leading to a SACM. The region of localized attack has been eliminated by Ni implantation which served to improve the nature of the passive film.

Galvanostatic Cathodic Plots

Cathodic kinetics were studied by galvanostatic polarization in 1N H_2SO4 saturated with H_2. The electrode was kept at -900 mV (SCE) for 30 minutes to remove any oxide present on the surface. The current was increased in steps of 20μA after every 2 minutes. The current and potential were plotted on a semi-logarithmic scale. The hydrogen exchange current density was

determined approximately by extrapolating the plot to 0.00 mV (SHE). The plots are shown in Figure 9.

Results and Discussion

The cathodic kinetic data are given in Table 5 for the implanted and unimplanted steels. Both the hydrogen exchange current density and the slopes are seen to markedly decrease with increase in nickel content, after 5% Ni is reached. This behavior is inconsistent with the fact that the hydrogen exchange current density of Ni is higher than that of Fe (14). Indeed, neither the exchange current densities nor the slopes are what might be expected from the conventional alloying behavior of Ni in Fe-Cr-Ni alloys (15).

From the previous discussion it has been established that the main features of the surface alloys is a high defect concentration with evidence of surface depletion of Cr. Topographically, selective sputtering has highlighted grains, according to the sputtering coefficient dependence upon grain orientation and inclusions.

In order to determine the effect specifically of defects upon the observed cathodic kinetics, a comparison was made between the cathodic kinetics of annealed 99.99% of pure Ni and the same material, self-implanted with a fluence of 4×10^{16} ion cm^{-2} at 150KeV to produce a comparable level of radiation damage. The curves are shown in Fig.10, and the kinetic parameters are given in Table 5. No significant change in slope or exchange current density for hydrogen is seen and only a small increase is observed in the current densities, which is easily attributable to surface roughening due to sputtering. Thus, in single phase Ni, radiation damage and sputtering has no major effect upon cathodic kinetics.

At this stage no model appears to be available to explain the above effects. For example, if one considers the enhancement of the surface area exposed of the carbides by sputtering, this would be expected to enhance the hydrogen reaction. In particular, radiation damage of the metal and carbide matrix might be expected to lead to easier carbon diffusion during implantation and partial carbide dispersal which would be expected again to enhance surface activity for the hydrogen reduction reaction. Such effects explain the increase observed in hydrogen kinetics of cold rolled steels (16, 17) over that of pure iron. The lowering of cathodic kinetics for the hydrogen reaction, therefore, requires further study.

Extrapolations of the cathodic plots to the corrosion potential have been carried out in order to determine the corrosion constant current, I corr. These values are also given in Table . The data indicates that some reduction in the corrosion rate may be attributed to the ion implantation process, as well as to the implantant species.

CONCLUSIONS

(1) It has been shown that improvements in general and localized corrosion resistance of 430 stainless steel in very aggressive aqueous media can be achieved by ion implantation with Ni to a depth of $\sim$ 500 Å.

(2) Some serious discrepancies exist between the calculated and the observed implantant distribution profiles. By far the most important cause of these discrepancies seem adequately explained by radiation-enhanced diff-fussion of Ni and Cr in opposite directions.

(3) The SACM produced in the anodic polarization of deaerated 1N H_2SO_4 is seen to diminish with Ni implantation. This is seen as evidence of the improvement in the composition and structure of the passive film formed in these regions due to Ni implantation.

(4) The cathodic kinetics of the Ni implanted steels do not follow conventional alloying trends. It is thought that impurity redistribution during implantation may play an important role in altering the kinetics of the hydrogen reduction reaction.

FIGURE CAPTIONS

Figure 1 Comparison of calculated (LSS) and observed (ESCA) distribution of Ni-implanted 430 stainless steel.

1a Curve (1): calculated profile for 1st implant and
Curve (2): calculated profile for 2nd implant
respectively for 15 At% Ni implant
Curve (3): resultant calculated profile
Curve (4): superimposed ESCA profile for Ni

1b Curve (1): single implant for 30 At% Ni implant
Curve (2): superimposed ESCA profile for Ni

Figure 2 Relative concentrations of chromium and iron in the region of implantation (points are joined by lines to show trends)
Curve (1): 5 At% Ni implant
Curve (2): 15 At% Ni implant
Curve (3): 30 At% Ni implant

Figure 3 Electron Micrographs and Selected Area Diffraction patterns for Ni-implanted 430 stainless steel, showing radiation damage of nickel rich BCC lattice

3a 15 At% Ni implant
3b 30 At% Ni implant

Figure 4 Relative concentrations of Fe^{3+}, Cr^{3+} and Ni^{2+} in air-formed oxide films on 30 At% Ni surface alloy

Figure 5 Active-Passive behavior of Ni-implanted and unimplanted 430 stainless steel in deaerated 1N H_2SO_4

Curve (1): 430 stainless steel
Curve (2): 5 At% implant
Curve (3): 15 At% implant
Curve (4): 30 At% implant

Figure 6 Pitting behavior of Ni-implanted and unimplanted 430 stainless steel in deaerated 1M NaCl

Figure 7 Galvanostatic cathodic plots for 430 and Ni implanted 430 in hydrogen saturated 1N H_2SO_4

Figure 8 Galvanostatic cathodic plots for pure Ni and self-implanted Ni in hydrogen saturated 1N H_2SO_4

REFERENCES

1. V. Ashworth, D. Baxter, W. A. Grant, and R. P. M. Procter, Corros. Sci., 16, 775 (1976).

2. V. Ashworth, D. Baxter, W. A. Grant, and R. P. M. Procter, Corros. Sci., 17, 947, (1977).

3. V. Ashworth, W. A. Grant, and R. P. M. Procter, Corros. Sci., 16, 661 (1976).

4. P. B. Needham, B. D. Sartwell and B. S. Covino, J. Electrochem. Soc., 125, 366 (1976).

5. B. S. Covino, P. B. Needham and G. R. Conner, J. Electrochem. Soc., 125, 370 (1978).

6. E. McCafferty and G. K. Hubler, J. Electrochem. Soc., 125, 1892 (1978).

7. J. Lindhard, J. M. Scharff and H. E. Schiott, KGL. DAN. VIC. SELSK. MATT-FYS. MEDD., 33, 14 (1963).

8. P. R. Okamoto and H. Wiedersich, J. of Nuclear Materials 53, 336 (1974).

9. J. E. Castle and C. R. Clayton, Passivity of Metals, Ed. R. P. Frankenthal and J. Kruger. (Proc. of Fourth Int. Symp. on Passivity, 1977), p. 714, Pub. Electrochemical Soc. Inc., Princeton, N. J. 1978.

10. W. D. France and N. D. Greene, Corrosion 24, 403 (1968).

11. C. D. Kim and B. E. Wilde, Corrosion Sci. 10, 735 (1970).

12. M. B. Rockel, Corrosion, 24, 95 (1971).

13. B. Mazza, Werkstoffe und Korrosion, 25, 239 (1974).

14. M. Pourbaix, Atlas of Electrochemical Equilibria in Aqueous Solutions, New York, Pergamon Press, 1966.

15. R. L. Beauchamp, Ph.D. Thesis, Ohio State University 1972.

16. Z. Foroulis, Sc.D. Thesis, Dept. of Metallurgy, MIT (1961).

17. H. H. Uhlig, Corrosion and Corrision Content, Wiley & Sons, 1963.

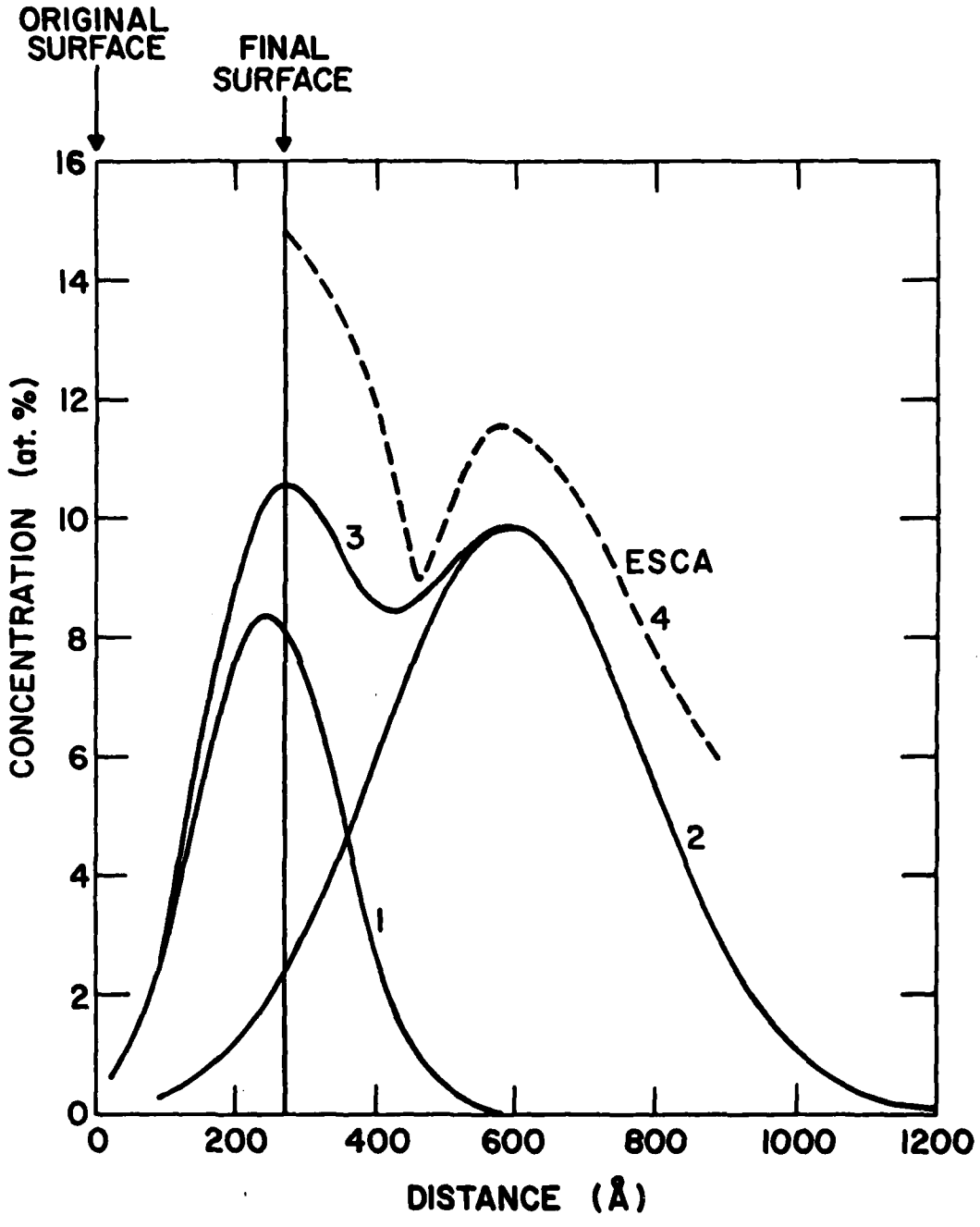
ORIGINAL SURFACE
FINAL SURFACE
CONCENTRATION (at. %)
DISTANCE (Å)
ESCA
1
2
3
4
0
2
4
6
8
10
12
14
16
0
200
400
600
800
1000
1200

Figure 1a

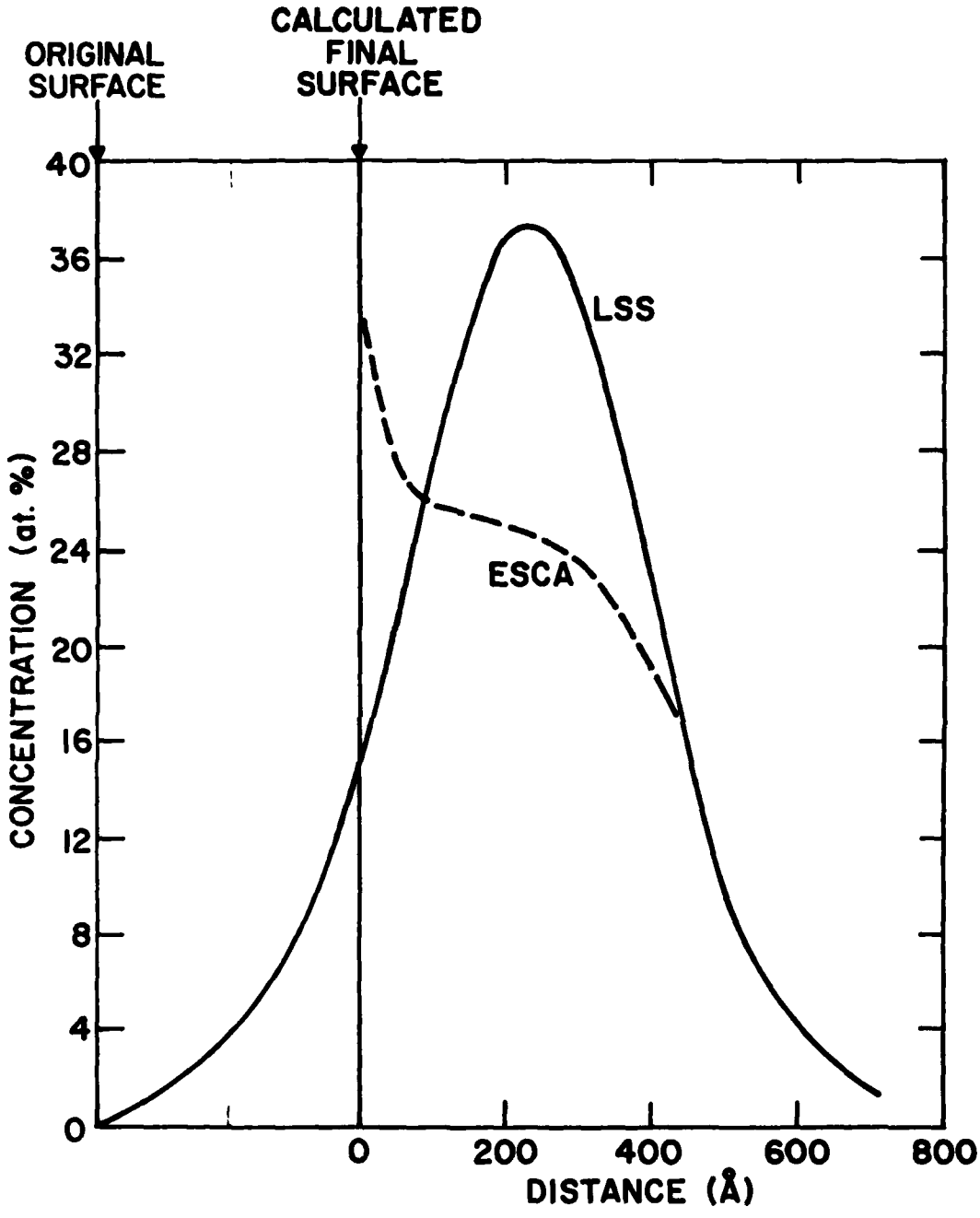
ORIGINAL SURFACE
CALCULATED FINAL SURFACE
LSS
ESCA
CONCENTRATION (at. %)
0
4
8
12
16
20
24
28
32
36
40
0
200
400
600
800
DISTANCE (Å)

Figure 1b

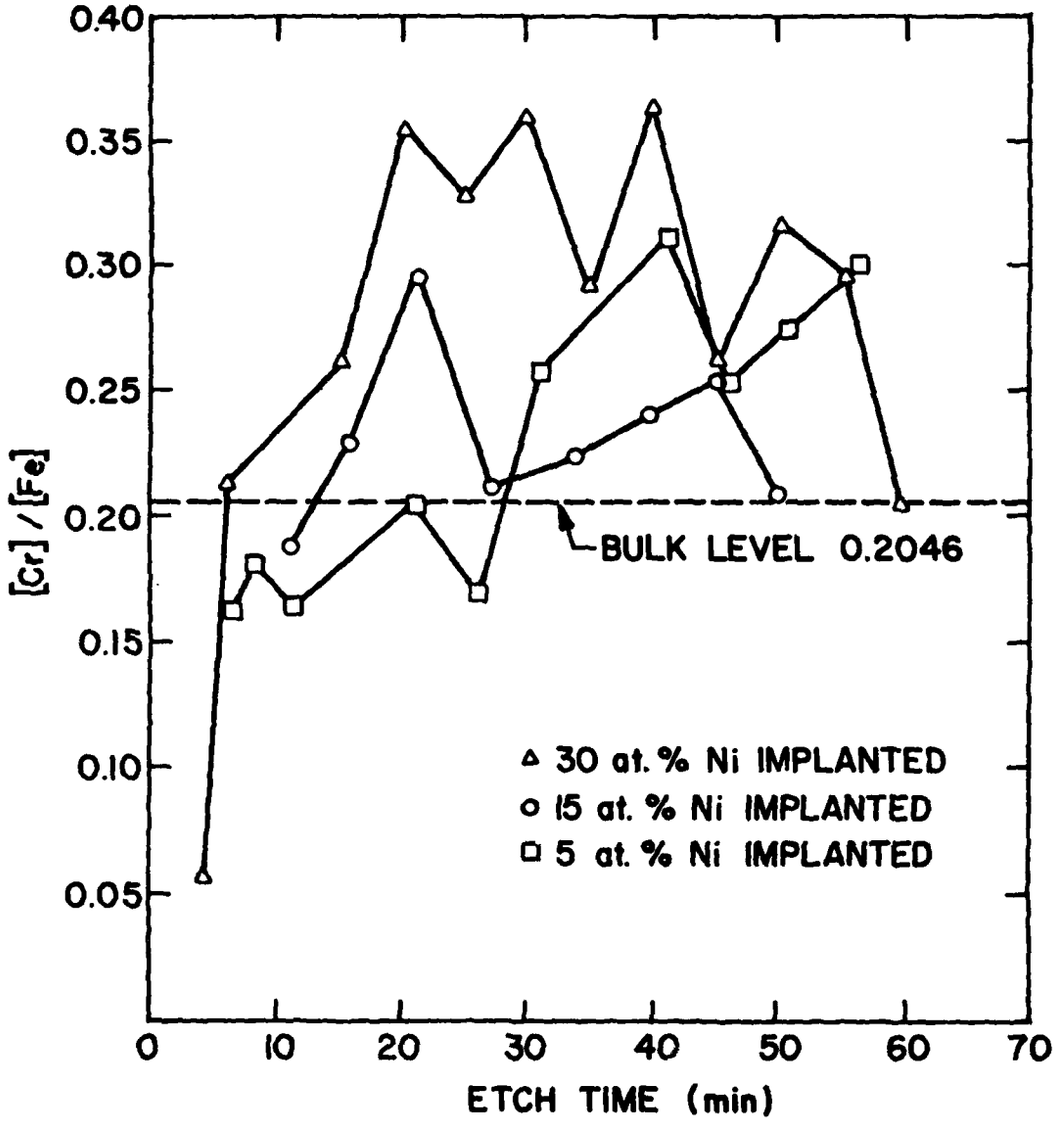
0.40
0.35
0.30
0.25
0.20
0.15
0.10
0.05
[Cr] / [Fe]
BULK LEVEL 0.2046
30 at. % Ni IMPLANTED
15 at. % Ni IMPLANTED
5 at. % Ni IMPLANTED
0
10
20
30
40
50
60
70
ETCH TIME (min)

Figure 2

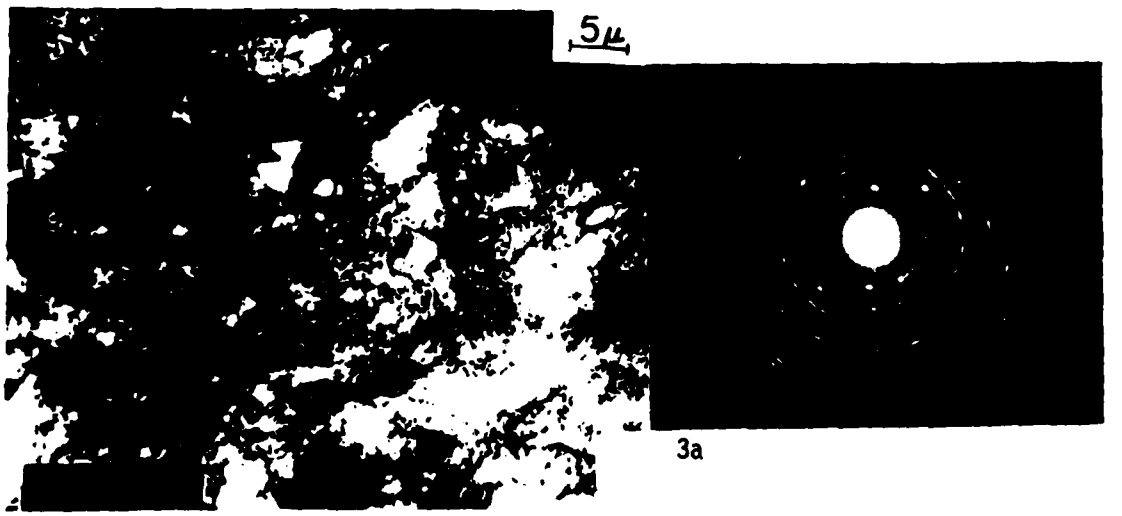

Figure 3

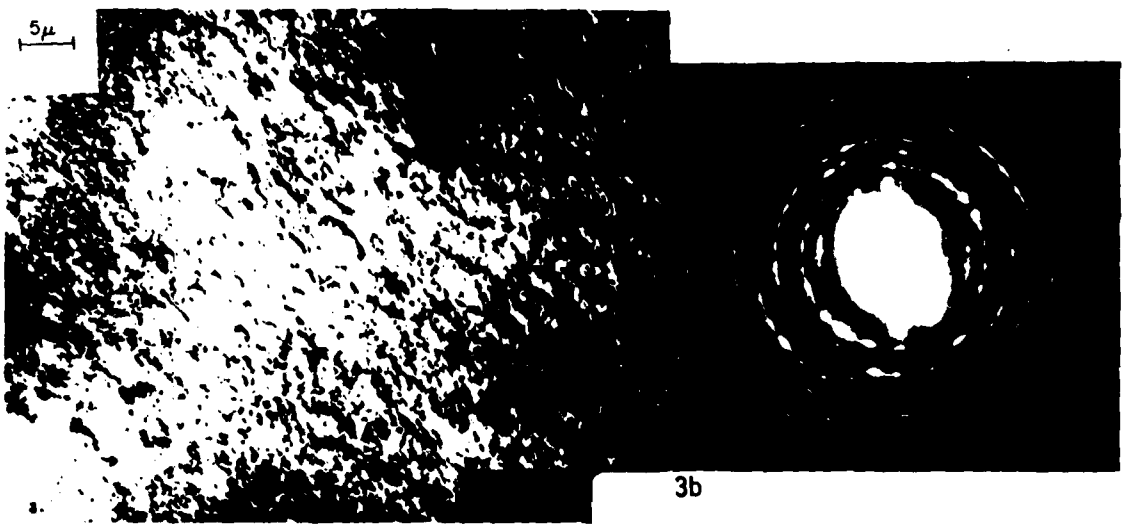

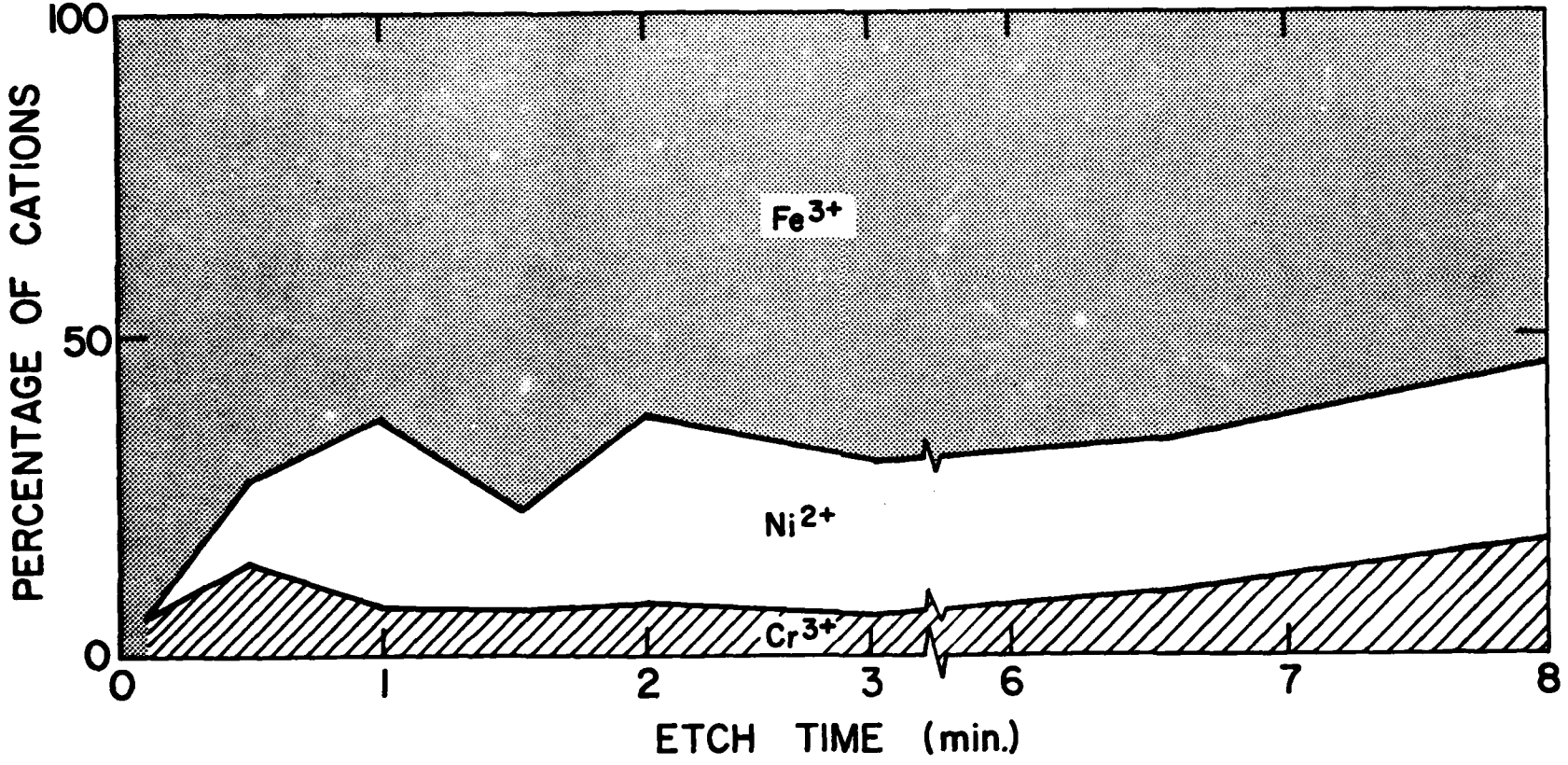
100
50
0
PERCENTAGE OF CATIONS
Fe^{3+}
Ni^{2+}
Cr^{3+}
0
1
2
3
6
7
8
ETCH TIME (min.)

Figure 4

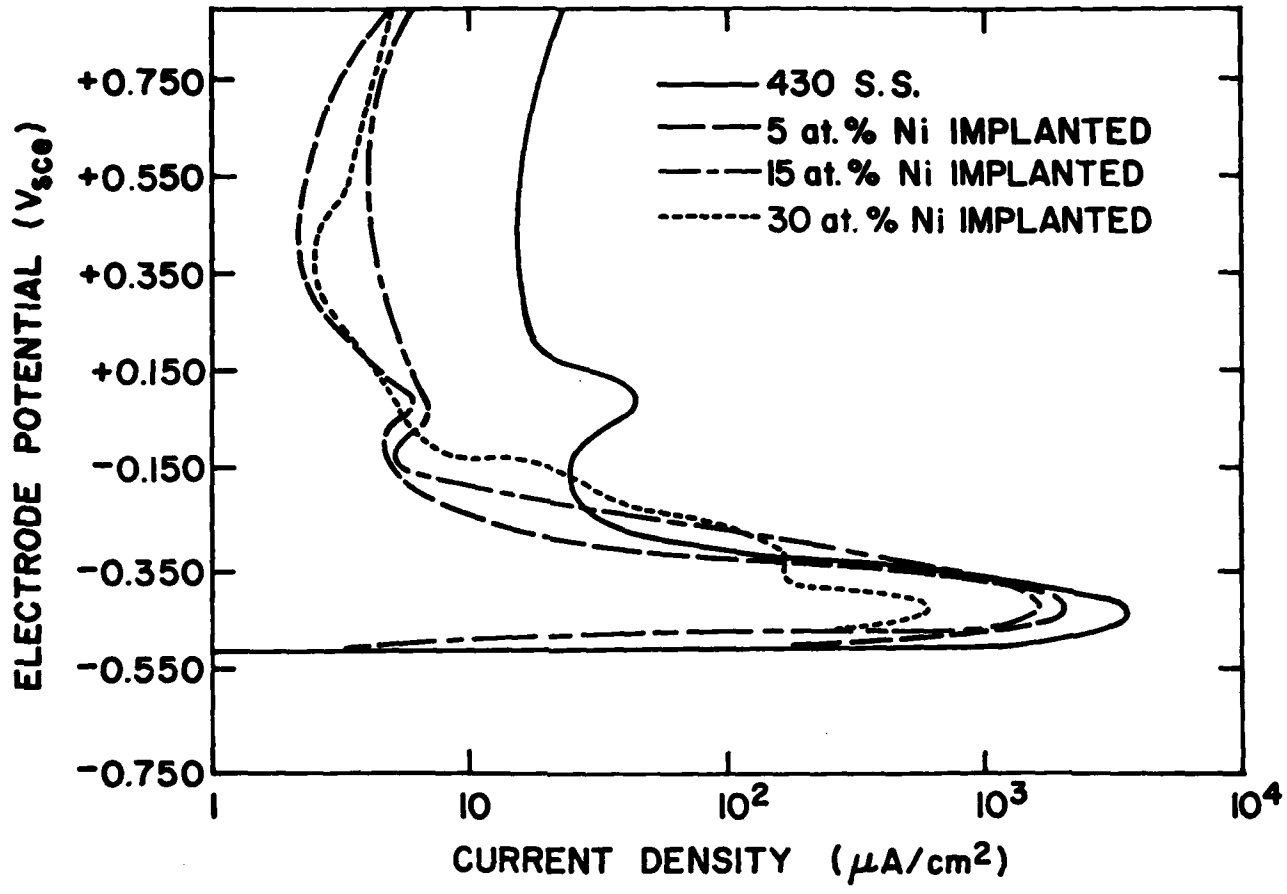
430 S.S.
5 at.% Ni IMPLANTED
15 at.% Ni IMPLANTED
30 at.% Ni IMPLANTED
+0.750
+0.550
+0.350
+0.150
-0.150
-0.350
-0.550
-0.750
ELECTRODE POTENTIAL (V_{sce})
1
10
10^2
10^3
10^4
CURRENT DENSITY ($\mu A/cm^2$)

Figure 5

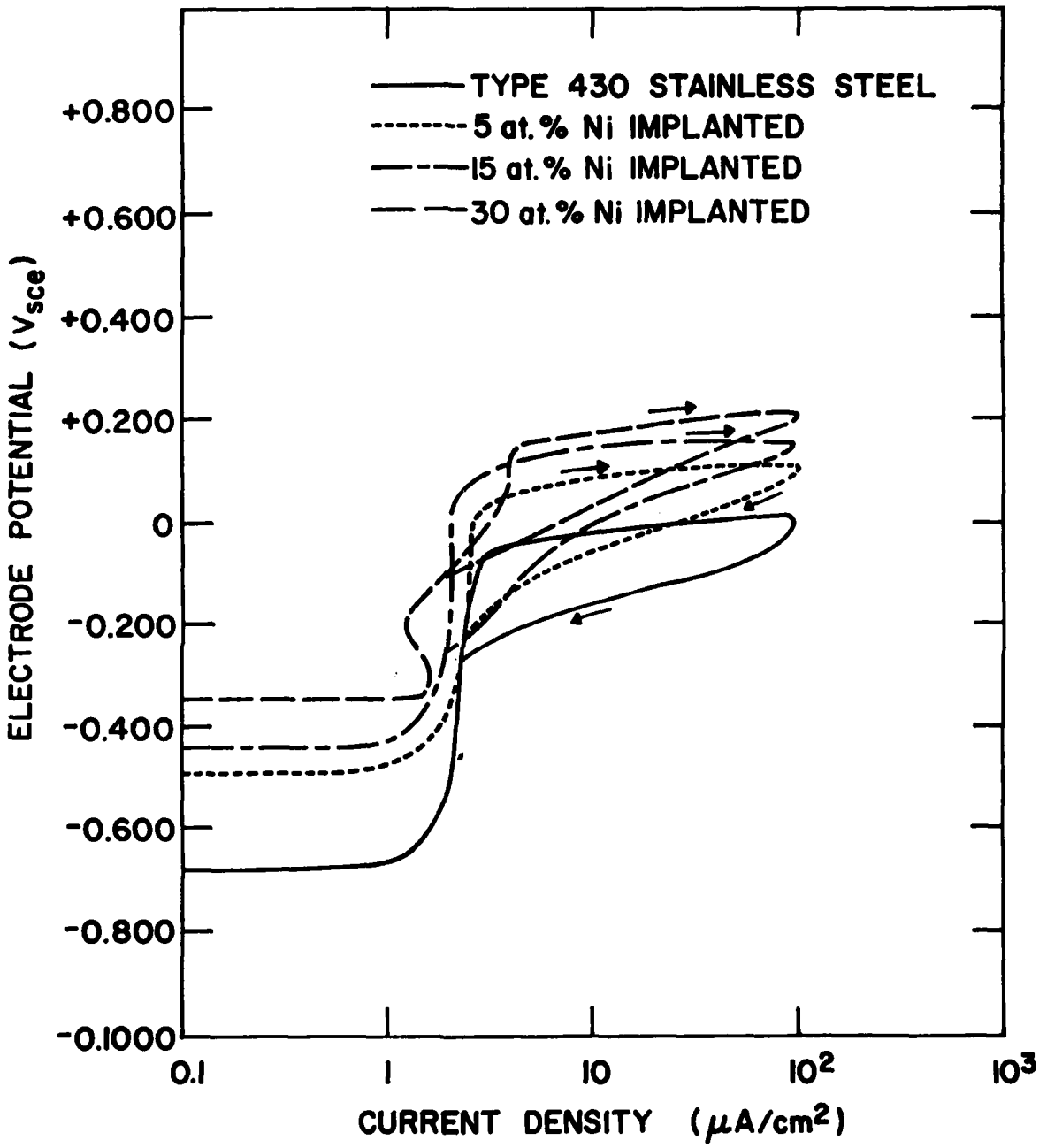
TYPE 430 STAINLESS STEEL
5 at.% Ni IMPLANTED
15 at.% Ni IMPLANTED
30 at.% Ni IMPLANTED
+0.800
+0.600
+0.400
+0.200
0
-0.200
-0.400
-0.600
-0.800
-0.1000
ELECTRODE POTENTIAL (V_{sce})
0.1
1
10
10^2
10^3
CURRENT DENSITY ($\mu A/cm^2$)

Figure 6

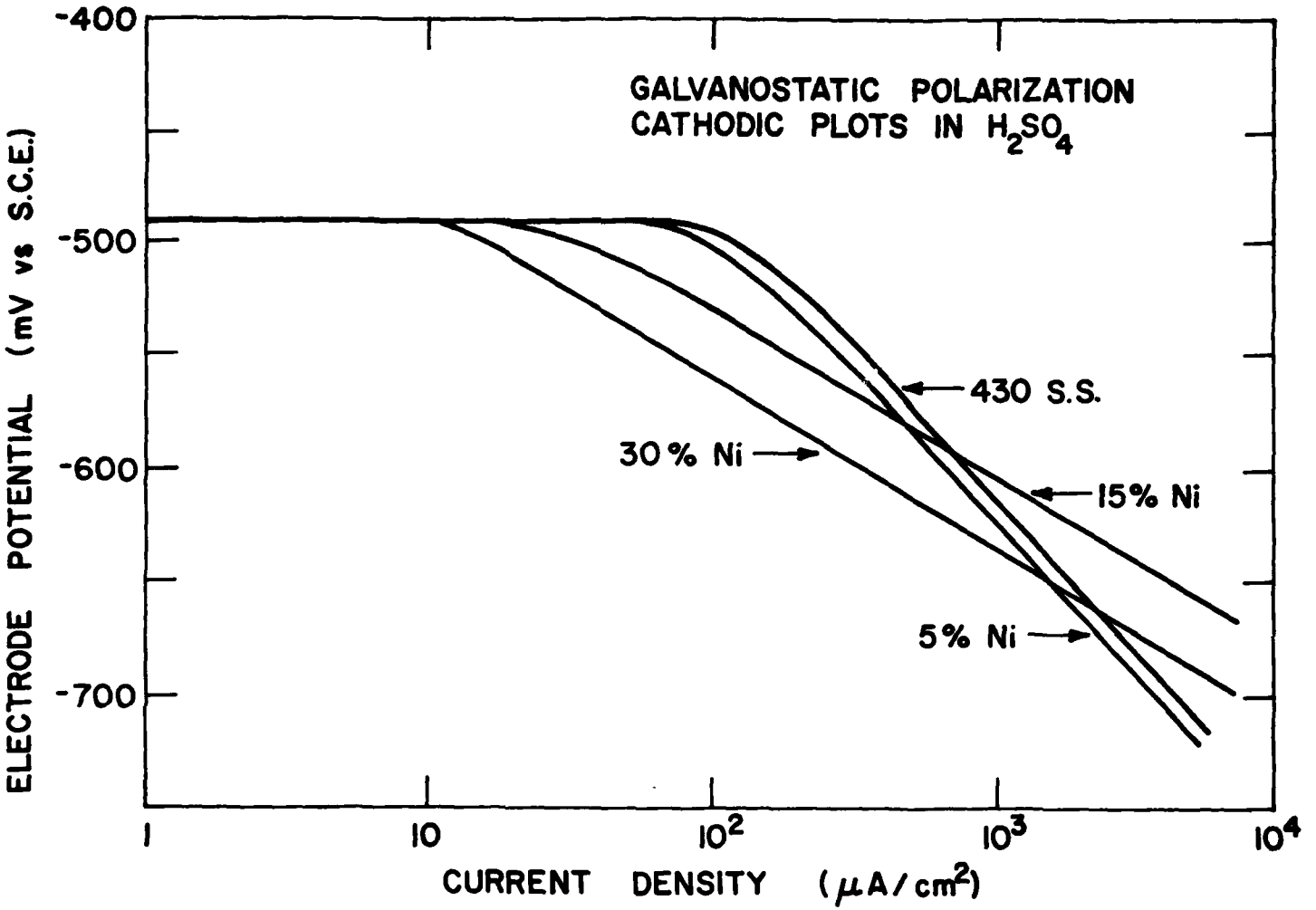
GALVANOSTATIC POLARIZATION
CATHODIC PLOTS IN H_2SO_4
-400
-500
-600
-700
ELECTRODE POTENTIAL (mV vs S.C.E.)
430 S.S.
30 % Ni
15% Ni
5% Ni
1
10
10^2
10^3
10^4
CURRENT DENSITY ($\mu A/cm^2$)

Figure 7

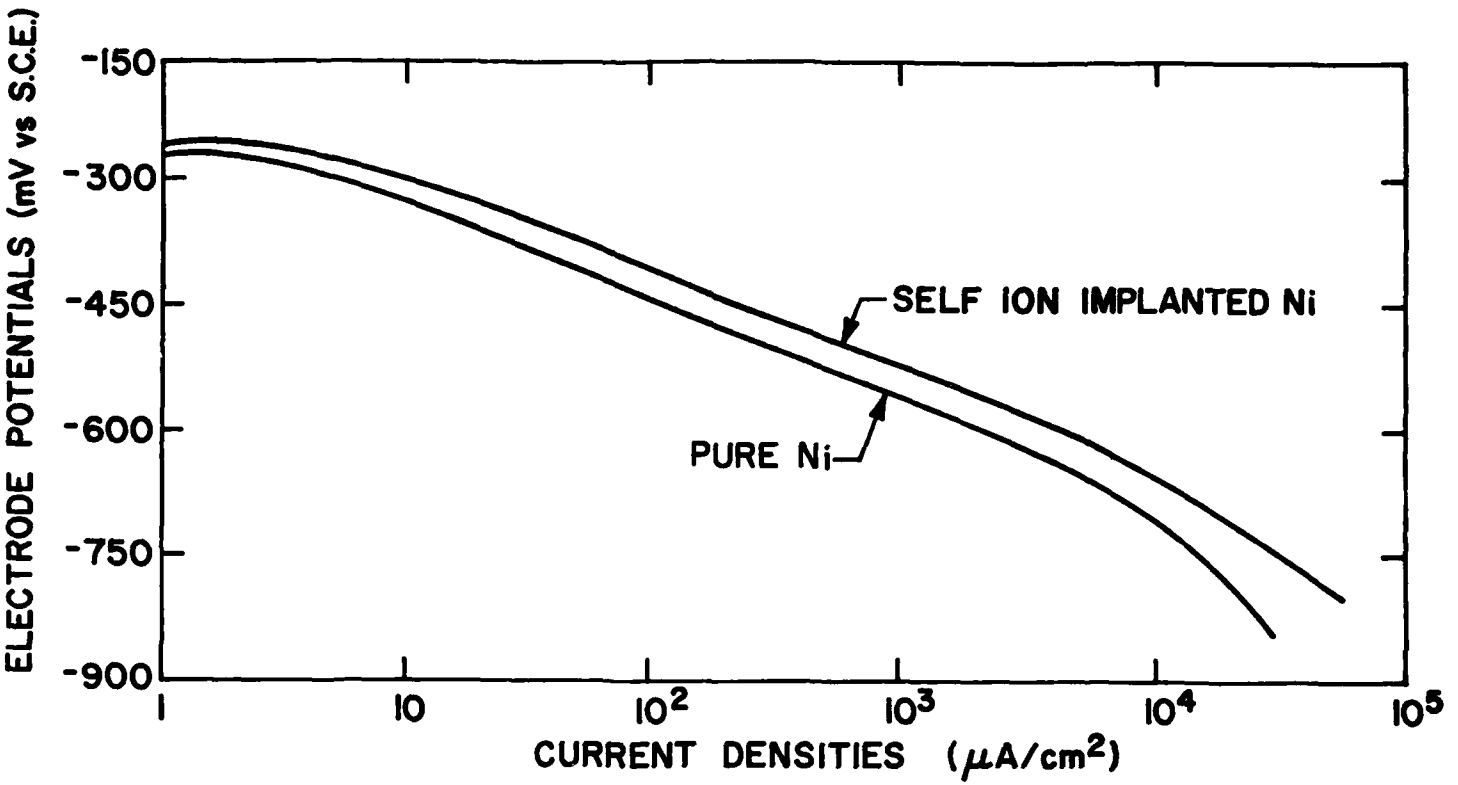
ELECTRODE POTENTIALS (mV vs S.C.E.)
-150
-300
-450
-600
-750
-900
1
10
10^2
10^3
10^4
10^5
CURRENT DENSITIES ($\mu A/cm^2$)
SELF ION IMPLANTED Ni
PURE Ni

Figure 8

TABLE 1

Composition of 430 Stainless Steel

% Cr	% C	% P	% S	% N
16.90	0.09	0.04	0.49	0.02

TABLE 2

Ion Implantation Parameters

MATERIAL	ENERGY (KeV)	FLUENCE IONS CM^{-2}
5% Ni	50	6.6×10^{15}
	150	2.2×10^{16}
15% Ni	70	1.8×10^{16}
	150	4×10^{16}
30% Ni	150	5×10^{17}

TABLE 3

MATERIAL	E_{ocp} (mV vs. SCE)	I_c ($\mu A/cm^2$)	E_{pp} (mV vs. (SCE)	I_p ($\mu A/cm^2$)
AISI type 430 S.S.	-490	3200	-415	14
5% Ni implanted Steel	-490	1200	-405	4
15% Ni implanted Steel	-490	600	-405	2
30% Ni implanted Steel	-490	450	-395	1.2

TABLE 4

MATERIAL	E_{ocp} (mV vs. SCE)	E_{pit} (mV vs. SCE)	E_{prot} (mV vs. SCE)
430 S.S.	- 684	- 60	- 260
5% Ni	- 492	0	- 240
15% Ni	- 444	+ 30	- 260
30% Ni	- 356	+100	- 140

TABLE 5

MATERIAL	bH(mV)	IoH_2(mA cm^{-2})	I CORR (mA cm^{-2})
430 ss	132	1.80×10^{-3}	1.07×10^{-1}
5% Ni	125	1.31×10^{-3}	9.40×10^{-2}
15% Ni	73	1.76×10^{-5}	2.60×10^{-2}
30% Ni	66	2.07×10^{-6}	1.60×10^{-2}
Pure Ni	116	3.50×10^{-2}	4.00×10^{-3}
Self-Ion Implanted	115	4.00×10^{-2}	3.25×10^{-3}

FATIGUE-LIFE ENHANCEMENT BY ION IMPLANTATION

Wen-Wei Hu, C.R. Clayton and H. Herman
Dept. of Materials Science & Engineering
State University of New York, Stony Brook, N.Y. 11794

and

J.K. Hirvonen
Materials Modification Branch, Naval Research Laboratory
Washington, D.C. 20375

Ion implantation is known to improve both mechanical and corrosion properties of a wide range of metals and alloys[1]. For example, wear rates of nitrogen-implanted steel can be considerably decreased[2]. And it has been reported that fatigue behavior can be improved by implantation[3]. However, to our knowledge there is no published data currently available demonstrating this effect. The present note gives preliminary results on the improvements of the fatigue behavior of steel by means of ion implantation of nitrogen.

The ion implantation of N_2^+ at 150 KeV has been employed to improve the fatigue life of a AISI 1018 steel. A rotating fatigue test, conducted at 5000 RPM, was employed to test standard fatigue specimens of circular cross-section, having a diameter of 9.53 mm and a gauge length of 25.4 mm, throughout the curved region [radius of curvature of 35.1 mm]. Nitrogen molecules were accelerated to 150 KeV and uniformly implanted into the rotating circular fatigue specimens to a fluence of 2×10^{17} N atoms/cm^2 in the central section. The temperature of the specimen during the implantation did not exceed 100°C, but did reach temperatures in excess of ambient during the course of the implantations ($\sim$ 1.5 H).

Following implantation, the specimen was either tested promptly or aged at room temperature or at slightly elevated temperatures. During the early stages of this study it became apparent that freshly implanted specimens

showed no consistent improvement of fatigue behavior. On the other hand, when the specimens were held at room temperature for several months prior to testing, there was a measurable improvement of fatigue life. This aging effect was confirmed by artificial aging for 6 hours at 100°C. The latter treatment was determined by calculating the diffusion distance for a nitrogen atom in ferrite during a period of 4 months at room temperature: 0.37 μm. The artificial aging treatment (6 h. at 100°C) was chosen to give the same diffusion distance.

The data are summarized schematically in Figure 1, where the number of cycles-to-failure is plotted schema cally for four different specimen treatments. The different symbols associated with the data presented in Figure 1 represent the three different rod stocks used. A stress level of 345 MPa was used for all but two experiments, where 373 MPa was employed. The nominal yield stress for 1018 steel is 373 MPa.

The overall trend is obvious from the figure. The as-received (non-implanted) specimens show a life-time of about 10^6 cycles, whereas the implanted (non-aged) specimens show a greater range of lifetimes as well as a trend to higher lifetime values (an average lifetime of 2.5×10^6 cycles for the six samples shown).

A clear improvement, however, appears for the aged specimens. The three implanted and room-temperature-aged specimens show no failure up to 10^8 cycles for the stress employed. For the case of artificial aging at 100°C, one specimen showed no failure up to 10^8 cycles and two others failed at 12×10^7 cycles and 6.9×10^6 cycles, respectively. We thus conclude that both natural (at room temperature) and artificial aging gives rise to improved fatigue behavior in 1018 steel.

Transmission electron microscopy examinations were initiated concurrently with these fatigue studies[4]. The as-implanted specimens appeared to contain a nitrogen martensite, but this was difficult to prove unequivocally. A

finely dispersed metastable nitride of $Fe_{16}N_2$ - type was also seen in the as-implanted specimens. Vogel has previously found carbon-martensite in carbon-implanted iron films[5].

The explanation of the aging effect must await the outcome of further, more detailed study, but preliminary explanations may be ventured. Aging gives rise both to the relaxation of high residual stresses, and to nitrogen diffusion to dislocations and to metastable nitrides. The as-implanted nitrogen will likely be limited to a region of approximately 0.1 micrometer from the surface, while aging will permit diffusion of nitrogen (e.g., into deeper regions of the specimen). At this stage it would be pure conjecture to attempt a detailed explanation of the observed effects. Further experimentation, including nitrogen profiling and further microstructural analysis are being carried out to better understand this improvement of fatigue lifetime by means of ion implantation

Portions of this work at Stony Brook were supported by a contract from the Office of Naval Research (N00014-77-C-0424).

References

(1) V. Ashworth, W.A. Grant, R.P.M. Procter and T.C. Wellington, Corros. Sci. 16, 393 (1976).

(2) G. Dearnaley and N.E.W. Hartley, AERE Harwell, AERE-R8562 (1976).

(3) N.E.W. Hartley, Inst. Phys. Conf. Ser. No. 28, 210 (1976).

(4) J. Kozubowski, W.W. Hu, C.R. Clayton, H.Herman and J.K. Hirvonen, to be published.

(5) F.L. Vogel, Thin Solid Films, 27, 369 (1976).

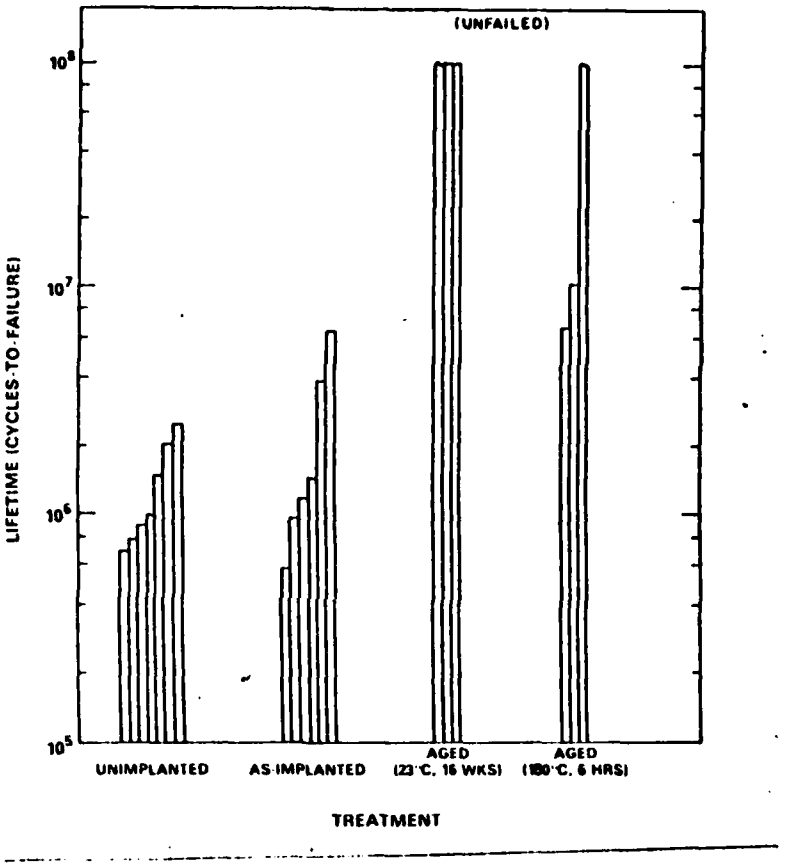

Figure 1. Influence of specimen treatment on fatigue fatigue lifetime of nitrogen-implanted type-1018 steel.

Transmission Electron Microscope Study of Nitrogen-Implanted 1018 Steel

SYNOPSIS

The structure of the near-surface layer of 1018 steel implanted with 150 keV nitrogen kons at a dose of 2×10^{17} ions/cm^2 was studied by means of transmission electron microscopy (TEM). The specimens, following implantation, were found to contain precipitates of metastable α'' ($Fe_{16}N_2$) iron nitride. These precipitates were much smaller and their density was greater than those produced in conventional nitriding.

Transmission Electron Microscope Study of Nitrogen-Implanted 1018 Steel

J.A. Kozubowski*, W.W. Hu**, C. R. Clayton**, H. Herman**, J.K. Hirvonen***

ABSTRACT

The structure of the near-surface layer of 1018 steel implanted with 150 keV nitrogen ions at a dose of 2×10^{17} ions/cm^2 was studied by means of transmission electron microscopy (TEM). The specimens, following implantation, were found to contain precipitates of metastable α'' ($Fe_{16}N_2$) iron nitride. These precipitates were much smaller and their density was greater than those produced in conventional nitriding.

* Department of Materials Science and Engineering, State University of New York at Stony Brook, on leave from the Institute of Materials Science and Engineering, Warsaw Technical University, Narbutta 85, 02-524, Warsaw, Poland.

** Department of Materials Science and Engineering, State University of New York at Stony Brook, Stony Brook, Long Island, N.Y. 11794, USA.

*** U.S. Naval Research Laboratory, Washington, D.C. 20375, USA.

INTRODUCTION

Nitrogen ion implantation represents a major departure from conventional ion nitriding. Ion implantation is a low temperature process in which bulk diffusion of nitrogen atoms is limited and conditions of surface diffusion and surface reactions are of secondary importance. In nitriding, on the other hand, surface reactions are of central importance and nitrogen bulk diffusion gives rise to layers of nitrides of different composition (1). An additional difference between these two processes is due to the fact that ion bombardment-induced damage can promote clustering of implanted atoms and nucleation of precipitates.

MATERIALS AND METHODS

A commercial 1018 steel, in the form of 9.5mm diameter rods, was the starting material. The mean grain diameter measured on the cross-section was estimated to be 30 μm, and the pearlite percentage was approximately 12%. Chemical analysis gave the following concentrations of the minor constituents: C(0.15-0.20%); Mn(0.6-0.9%); P(0.04%); S(0.05%).

The primary purpose of the study was to investigate the influence of nitrogen implantation on the fatigue properties of 1018 steel (2), and this motivation determined the method of surface preparation for the TEM specimens. Mechanical polishing of the surface to be implanted, followed by electropolishing of the back-side, was used in the preparation of thin foils suitable for TEM examination. Slices of 9.5 mm-dia. rods were; i) cut by an electrode discharge machine, ii) subsequently polished to obtain a 0.15 mm thickness, and iii) finally finished using 0.1 μm diamond paste. The samples were implanted with molecular nitrogen ions at an energy of 150 keV (75 keV per atom) to a fluence of 2×10^{17} N/cm^2 using an average

flux of ( ) ions $cm^{-2} \cdot s^{-1}$ at a temperature of <100°C. The maximum volume concentration of nitrogen atoms was estimated to be 30 at.%.

Jet polishing was employed to thin the specimens for TEM examination, using an electrolyte containing perchloric acid, ethanol and glycerine. Three kinds of specimens were used for the TEM study; i) unimplanted speciments, ii) specimens after ion implantation, and iii) the same specimens following annealing for six hours at 373°K.

EXPERIMENTAL RESULTS

The TEM results for unimplanted specimens are shown on Fig. 1a, 1b; and Fig. 2. A large density of dislocations is observed in ferrite grains with well-developed dislocations walls between subgrains. Similarly, the pearlite grains contain a large density of dislocations situated mainly at the cementite-ferrite interfaces.

Fig. 3a shows the structure following implantation. Here, interestingly, dislocation structures are no longer apparent. These implanted specimens give additional reflections (Fig. 3b), which are situated approximately midway between those originating from the ferrite. Dark-field micrographs made with the use of one of these extra reflections (situated close to the origin) reveal a large density of small precipitates: Fig. 3c. From the interplanar distance corresponding to the position of extra reflections closest to the origin of the diffraction pattern (0.42 nm and 0.40 nm), there is strong evidence for the presence of metastable iron nitride $Fe_{16}N_2$ (α'' in the nomenclature of Jack (3)). Angular positions of the other extra reflections and their relationship to the matrix spots agree with the α'' vs. α crystallographic relation

$[100]_{\alpha''}||[100]_{\alpha Fe}$; $(001)_{\alpha''}||(001)_{\alpha Fe}$ postulated by Jack (3) and confirmed by Pitsch (4). The shape of some matrix reflections which are visible in Fig. 3b is not round, but triangular (e.g., B-type reflection in Fig. 4). This is connected with the domination of one of three equivalent orientational variants $\{001\}_{\alpha}||\{001\}_{\alpha Fe}$ which give rise to a non-symmetrical distribution of double diffraction spots around matrix reflections of the {110}-type. The distribution of α" particles is not uniform, and the apparent decrease of their concentration towards the edge of the foil can be interpreted, apart from a pure thickness effect, to be due to a spatial distribution of α" particles which has a maximum value at some distance beneath the surface, with the density and sizes of the particles decreasing closer to the surface. The median size of the α" precipitates is estimated to be approximately 10 nm.

TEM pictures and selected area diffraction patterns do not provide conclusive evidence for the presence of nitrogen martensite (α') in the as-implanted material. Reflections which would originate from this phase should be situated close to the matrix spots, and are difficult to resolve since α" spots and double diffraction effects from the matrix cause considerable broadening of the matrix spots.

Specimens annealed after implantation (6h, 373°K) have a slightly different structure, as seen in Fig. 5ab. Additional contrast effects resembling acicular martensite are visible in the bright-field pictures (Fig. 5a) and on the dark-field pictures formed with the use of {110}-type matrix spots (Fig. 5b), but are invisible in the dark field pictures (Fig. 5c) formed with $Fe_{16}N_2$ spots. This contrast could be considered as evidence for the presence of nitrogen martensite, if it is noted that reflections from this phase are situated close to the matrix spots.

It is interesting to note the appearance of the large density of extremely fine, 2nm $Fe_{16}N_2$ precipitates visible in the dark field picture of the specimens annealed after implantation, in addition to the larger ones already present before annealing (Fig. 5c).

Fine linear contrast is also visible in the pearlite grains in the annealed specimens, Fig. 6; but in this case they are not so regular as in the ferrite grains (eg., Fig. 5a). There is undoubtedly some damage and defect formation in the cementite particles. However, the nature of this damage remains obscure due to the experimental difficulties in TEM observations.

DISCUSSION

At the outset, it is important to note that the material which was ion implanted consisted of two phases; ferrite and cementite, with the surface layer deformed by mechanical polishing. Phase non-uniformity, combined with the relatively low diffusion of nitrogen in iron at room temperature, will lead to different effects of ion implantation in the two phases. The observations reported here deal mostly with structural changes in the ferrite grains. Large numbers of defects which exist prior to implantation are expected to influence the kinetics of precipitation. For example, it is known that $Fe_{16}N_2$ nucleates at dislocations (5). If, in fact, there is a large dislocation density at the very beginning of nitrogen implantation, early nucleation of the metastable nitride, α'', might be expected.

Nucleation should be more or less uniform throughout the entire thickness of the implanted layer, with the restriction that the growth of precipitates in the region closest to the surface can be hindered by radiation damage and the thus-induced compressive stresses which have their maximum at some depth beneath the surface and close to the peak of the quasi-Gaussian

distributed implanted atoms. As was shown by Bhargava (6) and by Nakada (7), compressive stresses in excess to 90N/mm^2 will restrict the nucleation and growth of $Fe_{16}N_2$ precipitates. In this condition, one can expect to find larger precipitates of α" at some distance below the surface. This seems to be confirmed by the non-uniform distribution of α" particles in the TEM dark field micrographs, where the density and average size of the precipitates become smaller towards the edge of the foil, which in our case represents the surface of the implanted specimen. However, the decisive confirmation of this effect will only be obtained through the images of cross-sections.

The sizes, shapes and densities of the nitrides observed in this work are markedly different from those observed after conventional nitriding (8). Compared with nitriding, precipitates formed in ion-implanted material; i) are generally smaller, ii) do not have the usual platelet form, and iii) have much higher densities. The hardening due to such precipitates can be much greater than normally observed for the corresponding stage of aging in iron-nitrogen alloys. The apparent absence of primary and secondary dislocations (produced by implantation and diffusion processes) in the implanted layer is most probably caused by a large density of homogeneously distributed defects produced by high energy ions; in addition, some fraction of the deformation field of primary defects can be consumed by nucleation and growth of α" precipitates.

The formations of α" can be treated as an ordering process involving heterogeneous nucleation, especially in a structure having a large density of defects. The situation can be different in annealed material, where, for example, Garwood and Thomas (9) found a marked similarity between spinodal decomposition and the decomposition of nitrogen martensite. The implanted layers of 1018 steel which were studied in this work had large

quantities of primary and secondary defects. These defects promote early nucleation of α", which can thus be formed directly from the supersaturated solid solution of the implanted nitrogen in the iron matrix, in the absence of intermediate α' formation. This process is similar to that found in the decomposition of nitrogen-supersaturated ferrite (10). Moreover, it is reasonable to assume that the matrix containing a large density of implantation-generated defects, can accept a greater quantity of nitrogen atoms than could a perfect lattice in equilibrium conditions.

The presence of nitrogen martensite in the implanted material is not certain. Such martensites are usually formed during tempering of a quenched iron-nitrogen solid solution. However, if the structural unit of nitrogen martensite is considered to be a tetragonally-distorted α-iron unit cell, where the distortion is induced by nitrogen atoms randomly located in octahedral interstitial positions (3,11), then this phase might be expected to occur in nitrogen-implanted ferrite. The acicular contrast effects observed in the images of implanted samples after annealing for 6h at 373°K suggest that martensite may be present, but this does not represent decisive proof (these contrast effects cannot be interpreted as arising from Fe_4N precipitates either, since the corresponding diffraction patterns do not contain reflections from this phase). One can expect that analytical methods such as Mössbauer (12) or x-ray spectroscopy could provide a decisive answer as to the presence of nitrogen martensite in nitrogen-implanted ferritic steels.

SUMMARY

A large density of small (< 10 nm) metastable $Fe_{16}N_2$ (α") precititates is formed in the surface layer of N-implanted 1018 steel. TEM images of samples annealed for 6h at 373°K after implantation show martensite-like

contrast effects. However, additional evidence is needed to confirm the formation of nitrogen martensite in these samples. In addition to the α" precipitates observed in the as-implanted samples, a large quantity of smaller α" precipitates (~2 nm) were observed after annealing.

It can be concluded that high fuence nitrogen implantation of ferrite leads to the formation of metastable α" precipitates, occurring with a much higher density and with considerably smaller sizes than those formed with conventional ion nitriding. One can expect that the thin surface layer which contains a high density of fine α" precipitates and the excess nitrogen dissolved in defect structure will introduce pronounced changes in the fatigue properties of implanted samples. This, in fact, was found in a companion study, where nitrogen implantation and annealing of a 1018 steel gives rise to greatly extended lifetimes in high-cycle fatigue (2). Significant changes are expected to occur in other surface-dependent properties, such as wear, erosion and corrosion.

ACKNOWLEDGEMENT

This work was supported by the U.S. Office of Naval Research.

REFERENCES

(1) T. Sone et al., J. Japan Inst. Met. 40 (1976) 908.

(2) Wen-Wei Hu, C. R. Clayton, H. Herman and J. K. Hirvonen, Scripta Met. 12 (1978) 697.

(3) K. H. Jack, Proc. Roy. Soc. London 208 (1951) 216.

(4) W. Pitsch, Arch. Eisenhuttenwesen 32 (1961) 493.

(5) A. S. Keh and H. A. Wriedt, Trans. AIME 224 (1962) 560.

(6) R. D. Bhargava and D. McLean, J. Iron Steel Inst. 203 (1965) 699.

(7) Y. Nakada, W. C. Leslie and T. P. Churay, Trans. ASM 60 (1967) 223.

(8) G. R. Booker, J. Norbury and A. L. Sutton, J. Iron Steel Inst. 187 (1957) 205.

(9) R. D. Garwood and G. Thomas, Met. Trans. 4 (1973) 225

(10) P. Hayes, W. Roberts and P. Grieveson, Acta Met. 23 (1975) 849.

(11) N. DeCristofaro and R. Kaplow, Met. Trans. 8A (1977) 35.

(12) G. Longworth and N.E.W. Hartley, Thin Solid Films 48 (1978) 95, K. Yamakawa and F. E. Fujita, Met. Trans. 9A (1978) 91.

FIGURE CAPTIONS

Fig. 1 Structure of ferrite grain in subsurface layer of 1018 steel after mechanical polishing: (a) structure, (b) corresponding diffraction pattern with marked misorientations between subgrains.

Fig. 2 Structure of pearlite grain of 1018 steel after mechanical polishing.

Fig. 3 Structure of 1018 steel after ion implantation: (a) bright-field image, (b) selected area diffraction pattern, (c) dark-field image formed with the 101 α" spot marked on (b).

Fig. 4 Resolved selected area diffraction pattern: (•) A, matrix reflections broadened by precipitate reflections and double diffraction reflections, (▲) B, matrix reflections common with precipitate reflections, (·) C, $Fe_{16}N_2$ reflections.

Fig. 5 Structure of 1018 steel after ion implantation and low temperature annealing (6h at 373°K): (a) bright-field image, (b) dark field image formed with 110 matrix spot, (c) dark field image with 110 α" spot.

Fig. 6 Structure of pearlite grain in 1018 steel after ion implantation and low temperature annealing.

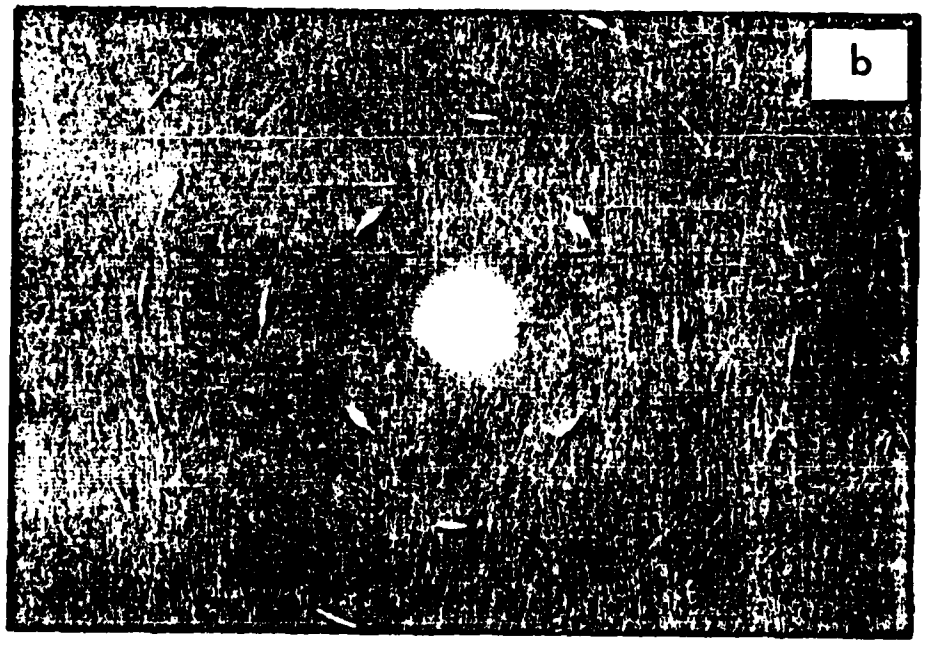

Fig 1

Fig 2

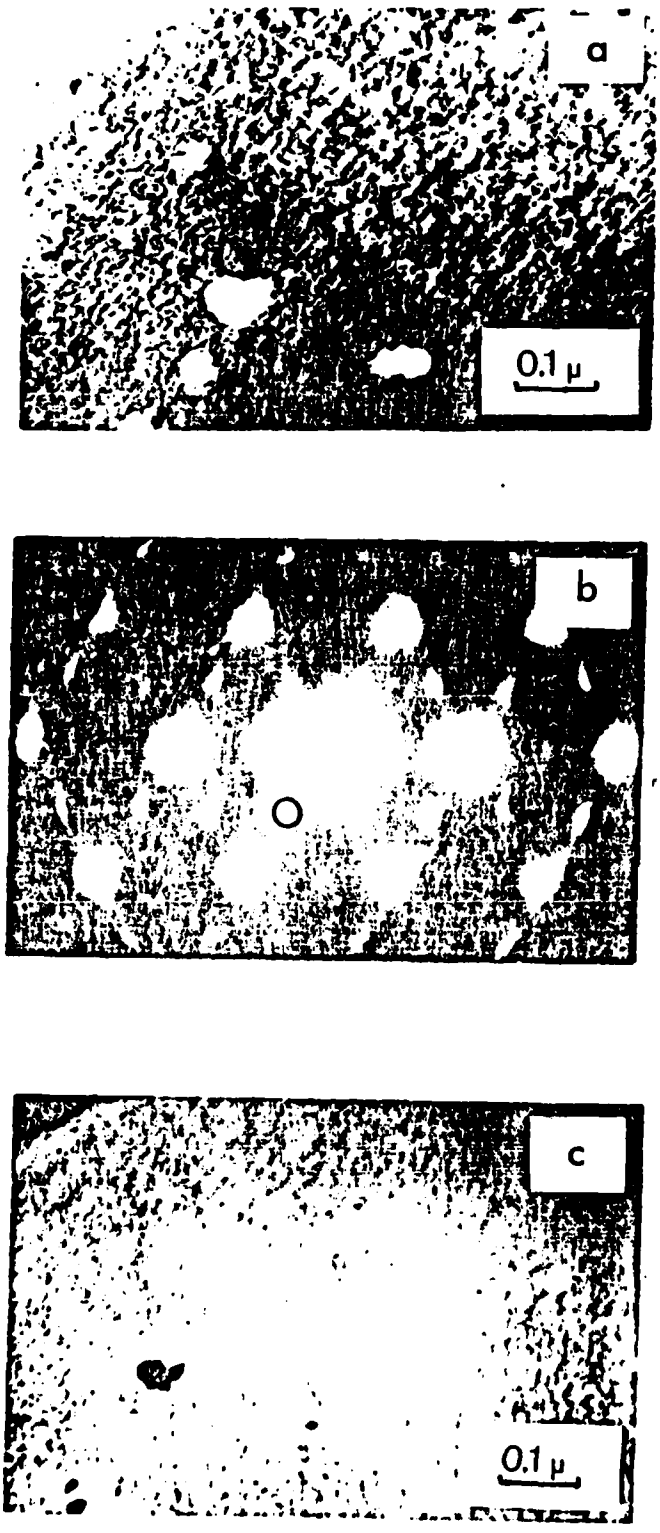

Fig 3

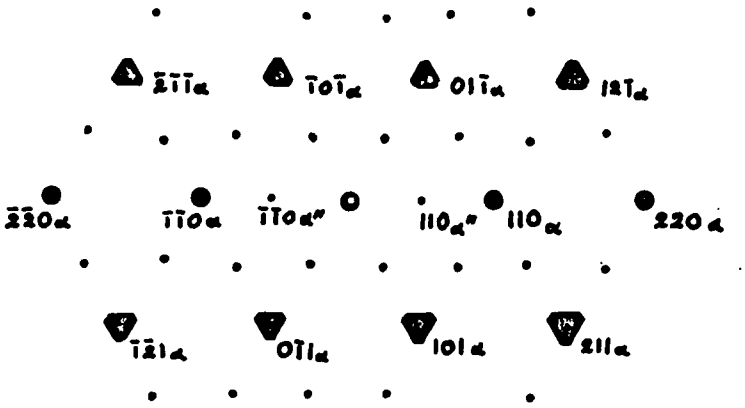
$\bar{2}\bar{1}\bar{1}_\alpha$
$\bar{1}0\bar{1}_\alpha$
$01\bar{1}_\alpha$
$12\bar{1}_\alpha$
$\bar{2}\bar{2}0_\alpha$
$\bar{1}\bar{1}0_\alpha$
$\bar{1}\bar{1}0_{\alpha''}$
$110_{\alpha''}$
110_α
220_α
$\bar{1}\bar{2}1_\alpha$
$0\bar{1}1_\alpha$
101_α
211_α

Fig 4

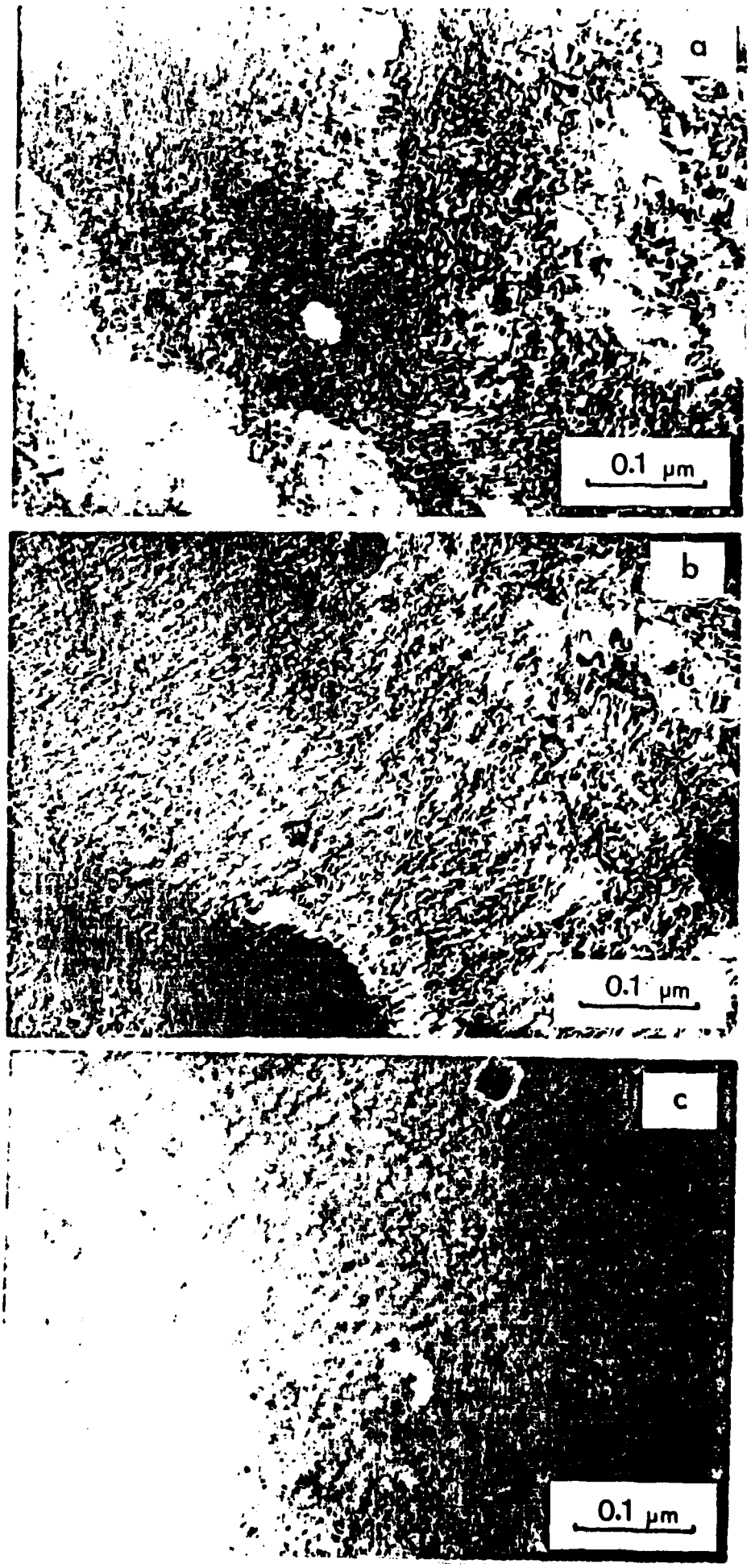

Fig 5

Fig 6

Cavitation-Erosion of Nitrogen-Implanted 1018 Steel

SYNOPSIS

The mechanical damage produced by ultrasonic cavitation-erosion in 150 keV nitrogen-implanted 1018 steel (0.18% carbon) was studied using weight loss measurements and SEM observations. Total weight-loss curves as a function of exposure time were obtained from three different samples. The results indicate that an induction period prior to damage is prolonged by $\sim$1.5 times through ion implantation and by a factor of 3 through ion implantation followed by aging. The surface roughness was observed to increase for continued cavitation exposure. The increase in incubation time and changes in topographical features are discussed in terms of formation of nitride and nitrogen martensite resulting from the implantation and aging.

INTRODUCTION

Ion implantation of 150 keV nitrogen has been employed to modify the mechanical properties of steel. It has been shown that both wear (1) and fatigue (2) properties can be improved. It has been previously observed in this program that aging (either naturally at room temperature or artificially at 100°C for 6 hours) of a 1018 steel which has been implanted, will result in significantly-enhanced high cycle fatigue lifetime (2). This has been related to diffusion-controlled implantant redistribution, which effectively gives rise to an improvement of surface-controlled mechanical properties. These results have been followed-up with TEM (3) and internal friction (4) studies.

Cavitation-erosion represents a dynamic degradation of a surface in the presence of a high density of collapsing bubbles. There are available standard laboratory tests which aim to simulate this commonly occuring industrial phenomenon.

In the present paper is described preliminary results on the response of ion-implanted 1018 steel to cavitation-erosion in distilled water.

EXPERIMENT PROCEDURE

Samples in three different conditions were studied in these experiments: (1) as-received; (2) following implantation to a nominal dose of $2 \times 10^{17} N/cm^2$ with nitrogen ions of 150 keV energy; (3) following implantation and aging at 100°C for 6 hours.

Accelerated cavitation-erosion was produced in distilled water by an ultrasonic vibratory probe, which is composed of a piezo-electric transducer and an exponentially-shaped horn. The frequency of this device is 20 KHz and the amplitude was maintained at 50 μm. The distance between the sample and horn was 0.635 mm.

In order to examine the change of surface topography with weight-loss on continuous exposure to cavitation, SEM photos were taken after different times of erosion.

RESULTS

Total weight-loss as a function of exposure time is given in Fig. 1. The incubation time, defined as the time of exposure prior to any detectable ($\leq$ 0.5 mg) weight-loss (5), for three experiments are given in Table 1.

Table 1

No. of Sample	Condition	Incubation Time
1	as-received	20 minutes
2	following implantation	33 minutes
3	following implantation and aging at 100°C for 6 hours	65 minutes

Since incubation time can be used as a comparative measure of erosion resistance, it is clear that cavitation resistance of 1018 steel has been significantly improved by implantation and aging.

Cavitation produces significant plastic deformation on an exposed surface. This is dramatically demonstrated in an examination of the cavitated-surface of sample 1 after 45 minutes of exposure, Fig. 2. In general, the initially smooth flat surface becomes undulated. Some small pits, attributed to the collapse of individual bubbles adjacent to the surface are observed. When the undulations become deeper, they develop into craters. Material is lost by ductile rupture from the rims of these craters (5), and thus voids can form below the rims (6).

In the present work, SEM showed different topographical features from sample to sample for the early stage of cavitation, i.e., in the first 120 minutes of erosion before the weight-loss became linear as a function of erosion time.

After 45 minutes of exposure, the grain boundaries between the ferrite and pearlite were delineated in samples (2) and (3), Fig. 3(a), 3(b). Also, cracks formed along the grain boundary and propagated into the ferrite. The lamellar structure of pearlite can be clearly identified due to the delineation and microcracking develops between the cementite and ferrite. Relative to samples (2) and (3), the former has a rougher surface, which can be seen at higher magnification, as illustrated in Fig. 4(a), (b). As for sample (1), neither the grain boundary nor the pearlite structure is visible, Fig. 2. The entire surface is rougher than sample (2) and (3). However, cracking is not visible.

After 90 minutes of exposure, sample (1) showed the roughest surface of the three; Fig. 5(a), where many voids are seen. Material is lost through the ductile rupture. Some regions which are comparatively undamaged, but with small pits on them, are believed to be pearlite grains. Sample (2) shows that most of the ferrite is lost under erosion attack, while pearlite grains can still be easily seen; Fig. 5(b). The latter observation would seem to show that pearlite is more resistant to cavitation-erosion than is ferrite. Sample (3) shows increased cracking in this period. Besides intergranular cracks, there are also transgranular cracks within the ferrite grain. The cracks become longer and wider due to propagation and the loss of material from their surroundings. These regions are mostly ferrite; Fig.5(c).

As cavitation proceeds beyond 120 minutes, after which considerable material has been removed, the surfaces of the samples is extremely rough. There is at these times little difference among the samples; Fig. 6(a), (b), (c).

DISCUSSION

Hardness is often cited as a measure of erosion resistance (7). It is known that an increase in strength by solid solution alloying or precipitation aging produces an increase in erosion resistance, together with a change in failure mode from ductile rupture to fatigue-like crack propagation (5).

From the present evidence of weight-loss and changes in surface topography it appears that the 1018 steel becomes harder following nitrogen implantation and aging at 100°C for 6 hours. There is TEM evidence from this laboratory that a very fine dispersion of metastable nitride results in 1018 steel when it is implanted with 150 keV nitrogen to a nominal dose of $2 \times 10^{17} N/cm^2$ (3). It can be calculated that the post-implantation aging schedule permits nitrogen to diffuse of the order of 4000Å, yielding a nitrogen martensite.

The presence of the high density of a nitride in the aged implanted material will limit the motion of near-surface dislocations. This results in confining the work hardening to a shallow surface layer (5). When the limit of plastic deformation and work hardening are reached, further energy input to the surface results in the initiation and propagation of cracks, which will eventually intersect and release erosion particles (8), as illustrated in Fig. 7. Erosion failure has generally been found to be transgranular (9). It is reported that in Ti-6Al-4V alloy such failure is a fracture process involving cracking along slip bands and interface, which is a common fracture path in fatigue (10). In addition, Hoff et al. have emphasized the importance of microstructure. They suggested that cracks can be initiated by the pile-up of dislocations (11). To prevent or delay this inhomogeneous dislocation pile-up, it is necessary to reduce dislocation mobility by providing a large number of very fine homogeneously dispersed

obstacles. The obstacles can be precipitates, grain boundaries, or martensite needles. Thus, material containing a fine dispersion of hard particle in a more elastic and ductile matrix should offer good erosion resistance (11).

The fracture process of fatigue and cavitation erosion for alloy of high solute content are in some ways similar. Both have to do with the formation and propagation of cracks. It is suggested that microstructures which result in long fatigue life also result in higher erosion resistance (8).

CONCLUSION

Nitrogen implantation can improve the cavitation erosion of 1018 steel. The result is consistant with the recent observations of enhancement of high cycle fatigue life by nitrogen implantation (2). A more recent study on internal friction indicates that following implantation, the internal friction decreases by 1/2 and the modulus increase measurably (4). These results are indicative of the formation of metastable nitrides and their interaction with near-surface dislocations.

A further more detailed report of these and other results is under preparation.

ACKNOWLEDGEMENT

This research at Stony Brook was sponsored by the U.S. Office of Naval Research Laboratory.

FIGURE CAPTIONS

Fig.1 Total weight loss vs time of exposure to cavitation for three different samples: as-received, following implantation and following implantation and aging.

Fig. 2 Plastic deformation formed on the surface of as-received sample after exposure to cavitation for 45 minutes.

Fig.3 Surface topography of following implantation and following implantation and aging sample after exposure to cavitation for 45 minutes: (a) following implantation, (b) following implantation and aging.

Fig. 4 Higher magnification of Fig. 3 (a), (b) showing following implantation (a) has a rougher surface than following implantation and aging (b).

Fig. 5 Surface topography of three samples after exposure to cavitation for 90 minutes: (a) as-received, (b) following implantation and (c) following implantation and aging.

Fig. 6 Surface topography of three samples after exposure to cavitation for 175 minutes: (a) as-received, (b) following implantation and (c) following implantation and aging.

Fig.7 Initiation and propagation of cracks in the following implantation and aging sample after exposure to cavitation for 28 minutes.

REFERENCES

(1) G. Dearnaley and N.E.W. Hartely, AERE Harwell, AERE-R8562 (1976).

(2) W.W. Hu, C.R. Clayton, H. Herman and J.K. Hirvonen, Scripta Met. 12 (1978) 697.

(3) J.A. Kozubowski, W.W. Hu, C.R. Clayton, H. Herman and J.K. Hirvonen (to be published).

(4) W.W. Hu, C.R. Clayton, H. Herman, R.K. MacCrone, R. Kant and J.K. Hirvonen, (to be published).

(5) S. Vaidya and C.M. Preece, Met. Trans. 9A (1978) 299.

(6) B. Vyas and C.M. Preece, Met. Trans. 8A (1977) 915.

(7) J.M. Hobbs and D. McCloy, Metals and Mater. 6 (1972) 27.

(8) Sheila Prasad, Master Thesis, S.U.N.Y. at Stony Brook (1976).
M.S. Plesset and A.T. Ellis, Trans. ASME 77 (1955) 1055.

(9) G.M. Wood et. al., J. Basic Engineering, Trans. ASME 890 (1967) 98.

(10) D. Essenmacher, M.F. Prozkop, D.E. Mikkola and D.A. Koss, Met. Trans. 9A (1978) 1069.

(11) G. Hoff, et.al, ASTM STP 408 (1967) 42.

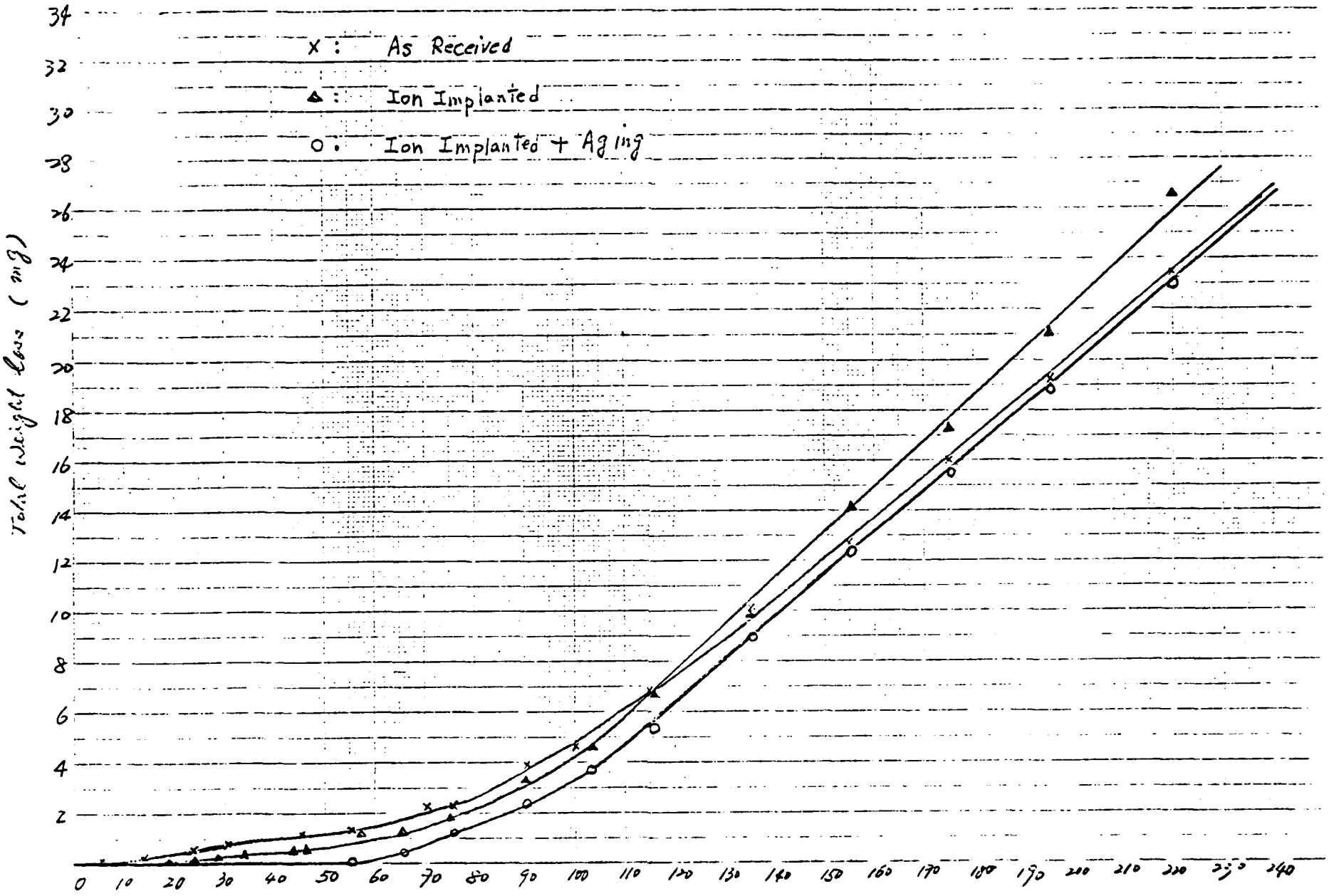
x : As Received
▲ : Ion Implanted
○ : Ion Implanted + Aging
Total Weight Loss (mg)
Time (min)
0 10 20 30 40 50 60 70 80 90 100 110 120 130 140 150 160 170 180 190 200 210 220 230 240
2 4 6 8 10 12 14 16 18 20 22 24 26 28 30 32 34

Fig 1

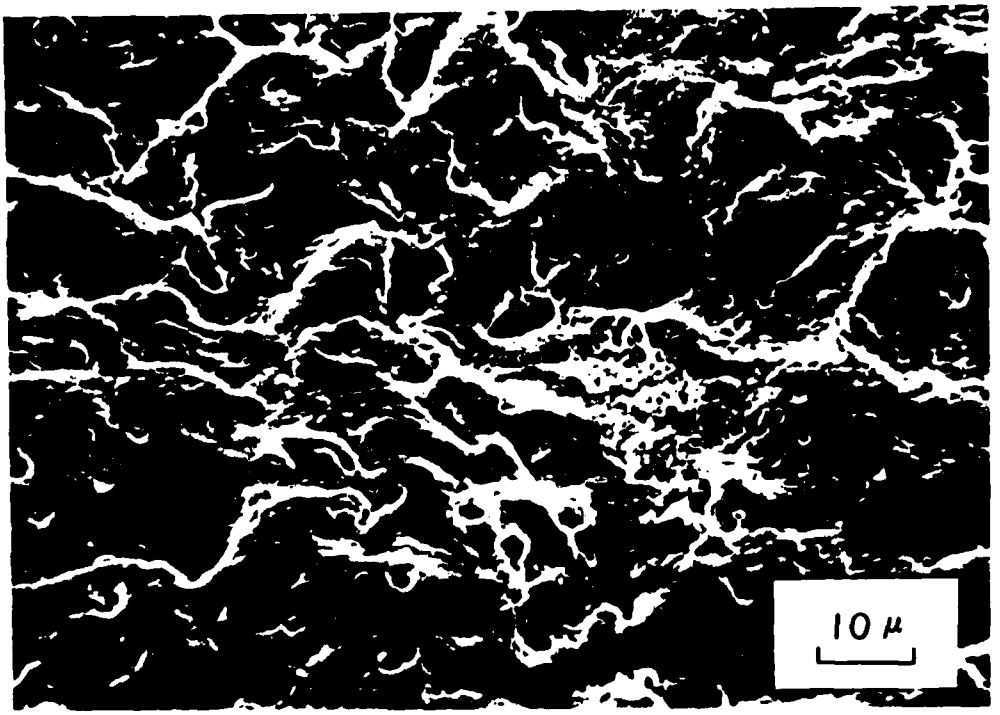

Fig. 2

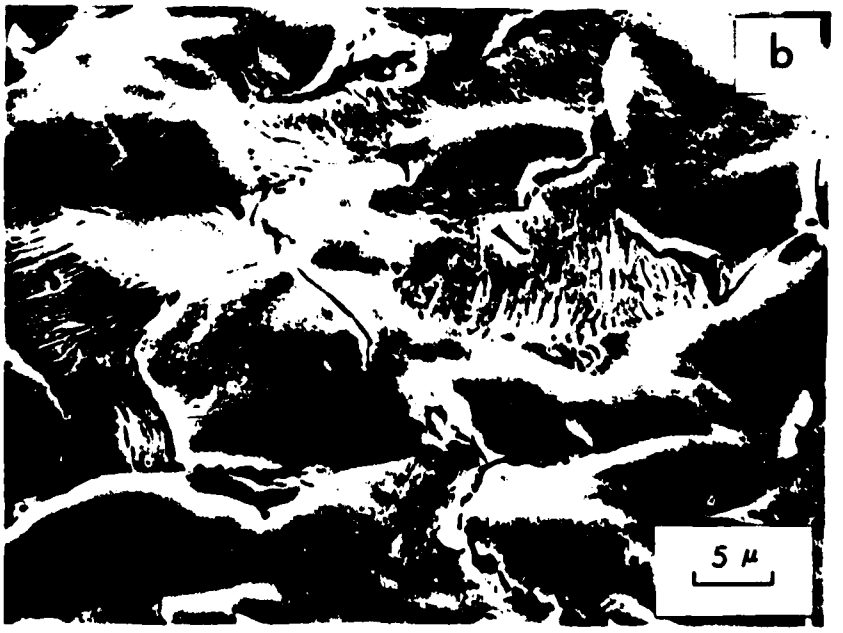

Fig. 3

Fig. 4

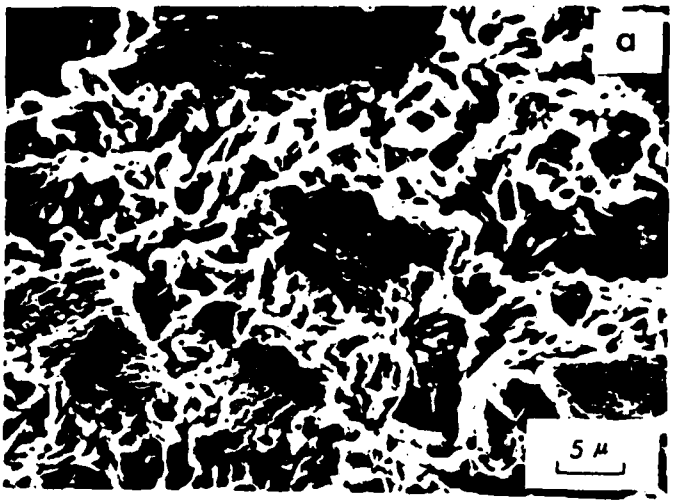

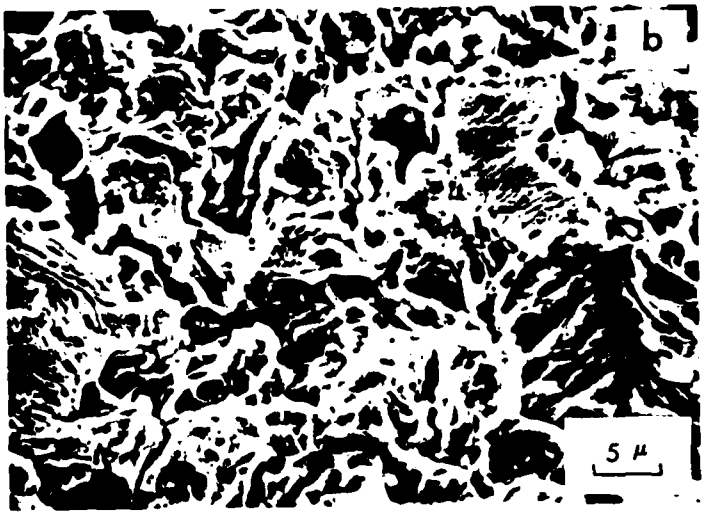

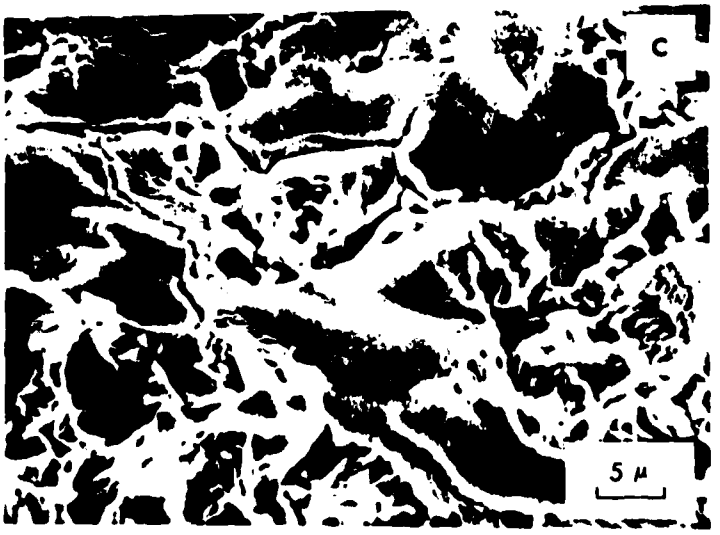

Fig. 5

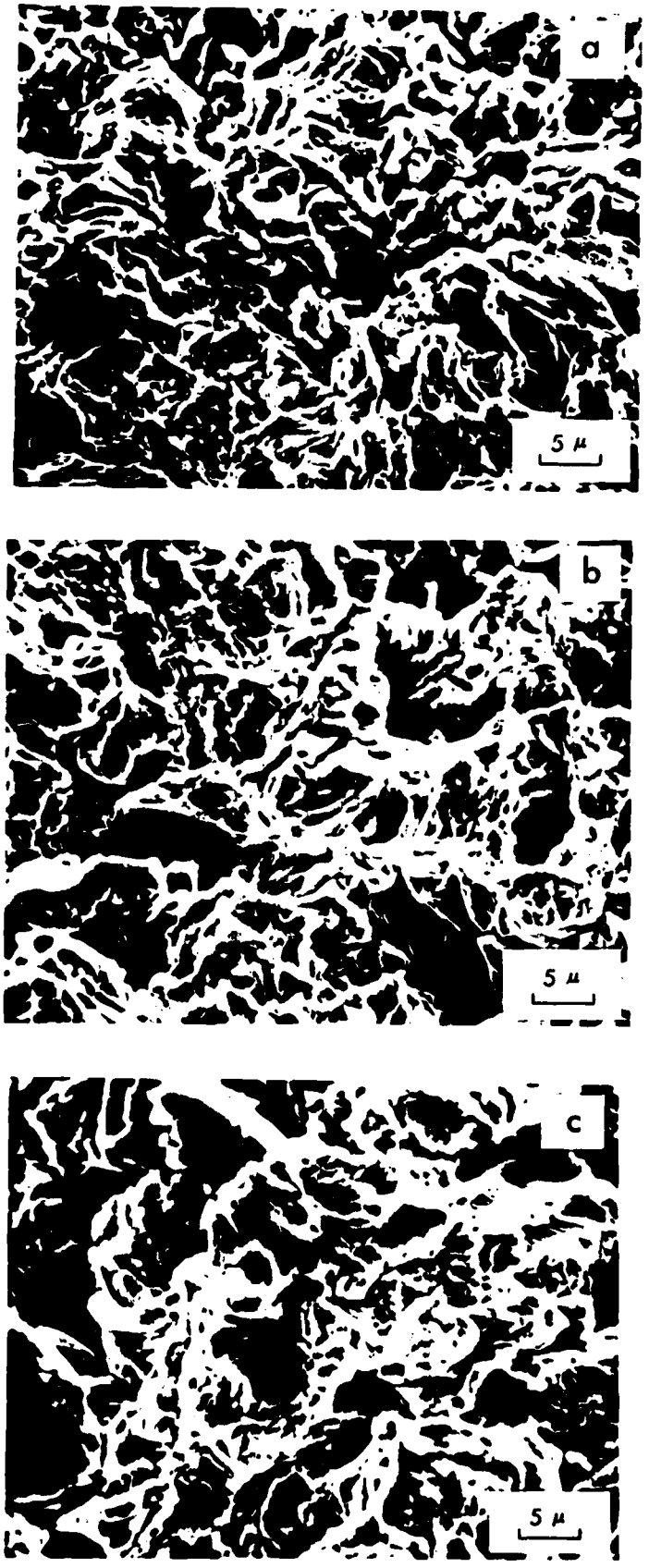

Fig. 6

Fig. 7

ANELASTICITY OF NITROGEN-IMPLANTED 1018 STEEL

Introduction:

Internal friction is an extremely sensitive method for studying the imperfections in crystalline solids (eg., interstitials and dislocations). The idea of measuring internal friction and modulus of nitrogen-implanted 1018 steel arose when it was found that both fatigue (1) and cavitation-erosion (2) behavior were significantly improved by nitrogen implantation. The modification of these surface-related mechanical properties are related to the motion of near-surface dislocations which is impeded by nitrogen-Cottrell atmospheres.

Experimental:

The material used in this experiment was cold-rolled AISI 1018 steel. Samples, which were made from a 9.53 mm diameter rod were fabricated to the shape shown in Fig. 1. Three samples with different conditions were studied: (a) as-received, (b) following implantation into both sides of the sample by 150 KeV nitrogen to a nominal dose of 2×10^{17} $N+/cm^2$ and (c) following the above implantation and aging at 100°C for 6 hours.

The internal friction measurement apparatus is shown schematically in Fig. 2. The resonance frequency of the specimen was detected by an oscilloscope used as a null detector. The resonance frequency was measured while the specimen was cooled from ambient to the temperature of liquid nitrogen (77°K).

The internal friction method devised for this study was due to a design of R. K. MacCrone and carried out cooperatively with him. In this method the central vibrating arm of the system is actuated by the excitation of a small piece of ferrite glued to the tip of that arm. Pickup was accomplished on the opposite side of the tip of the vibrating arm by a capacitive scheme.

The input frequency is varied and the output capacitive voltage is monitored. This design decreases to a minimum background noise which is normally a major limitation in highly sensitive measurements such as those performed here. It is to be recalled that we are attempting to detect effects of the presence of interstitial nitrogen at depths of the order of hundreds of Angstrons. It is also important to note that the strain employed here is less than 10^{-6} cm/cm.

The experiment is carried out by passing the system through resonance. When the square of the amplitude (X_0^2) is plotted against frequency, as shown in Fig. 3, two frequencies W_1 and W_2 are found at which X_0^2 falls to one-half the value of X_0^2 max. The internal friction is given by:

$$Q^{-1} = \frac{W_2 - W_1}{W_r}$$

where W_r is the resonance frequency.

In this preliminary work the internal friction was measured only at room temperature and at temperature of liquid nitrogen.

Result:

It was found that the resonance frequency increased as the samples were cooled from room temperature to 77°K. Fig. 4 shows that a square of relative resonance frequency ($(f_t/f_{77})^2$) plotted as a function of temperature, where f_{77} is the resonance frequency at 77°K and f_t is the resonance frequency at the temperature between 298°K and 77°K. It was seen that the implanted sample has a higher value of $(f_t/f_{77})^2$ than the as-received sample and the effect became more significant when the temperature is above 220°K. The modulus, which is proportional to the square of resonance frequency (3), will increase on nitrogen implantation.

The internal friction of the three different samples measured at room temperature and 77°K are listed in Table 1.

It is shown that following implantation, the internal friction decreased by ~1/2 as measured at room temperature and ~1/4 as measured at 77°K.

Aging after the sample was implanted did not give significant change either in modulus or internal friction.

This work is continuing, but a preliminary significant conclusion can be offered at this time. The decrease in internal friction following implantation can be related to the establishment of Cottrell atmospheres. This model is consistent with the previous results obtained in this program on surface-related mechanical properties, where both fatigue and corrosion-erosion properties are improved.

This work will be continued cooperatively with R. K. MacCrone of RPI and workers at NRL.

TABLE 1

Sample	Q^{-1} at R.T.	Q^{-1} at 77°K
as-received	1.675×10^{-3}	0.732×10^{-3}
following implantation	0.985×10^{-3}	0.55×10^{-3}
following implantation and aging at 100°C for 6 hours	0.835×10^{-3}	0.53×10^{-3}

References:

(1) W. W. Hu, C. R. Clayton, H. Herman and J. K. Hirvonen, Scripta Met., 12, 697 (1978).

(2) W. W. Hu, C. R. Clayton, H. Herman and J. K. Hirvonen (to be published).

(3) A. S. Nowick and B. S. Berry, An Elastic Relaxation In Crystalline Solids, Academic Press (1972), P. 19.

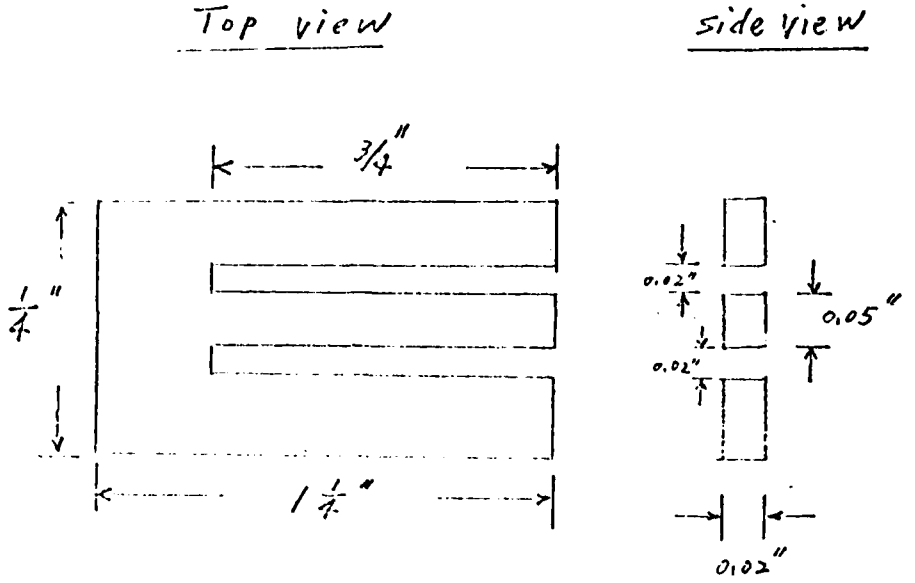

Fig 1

scale : inch

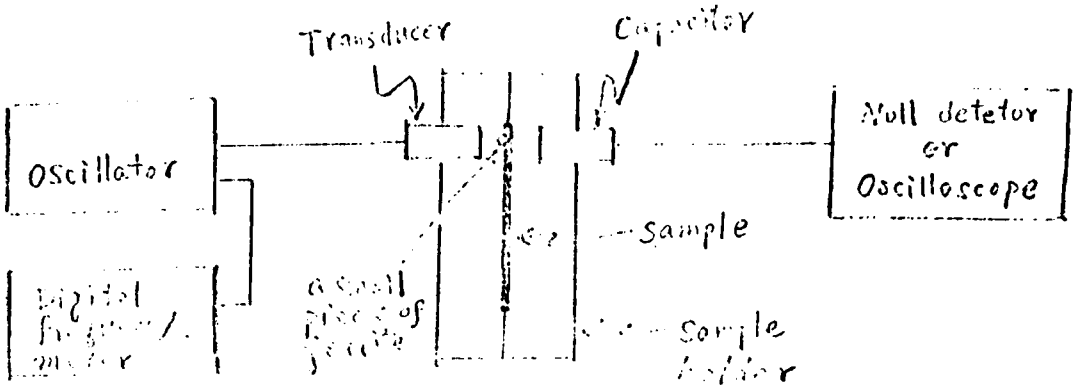
Transducer
Oscillator
Null detetor
or
Oscilloscope
Sample

Fig 2.

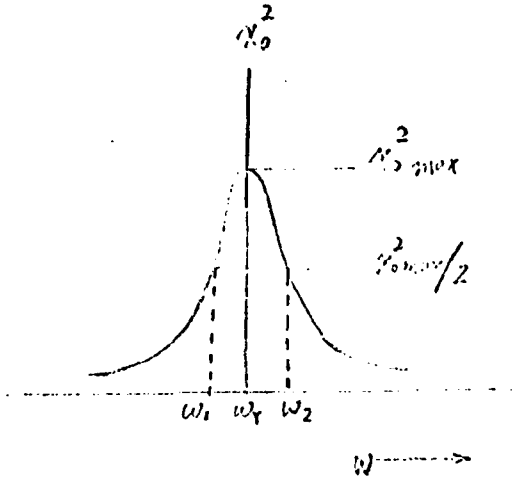
ω_1 ω_r ω_2
ω

Fig 3

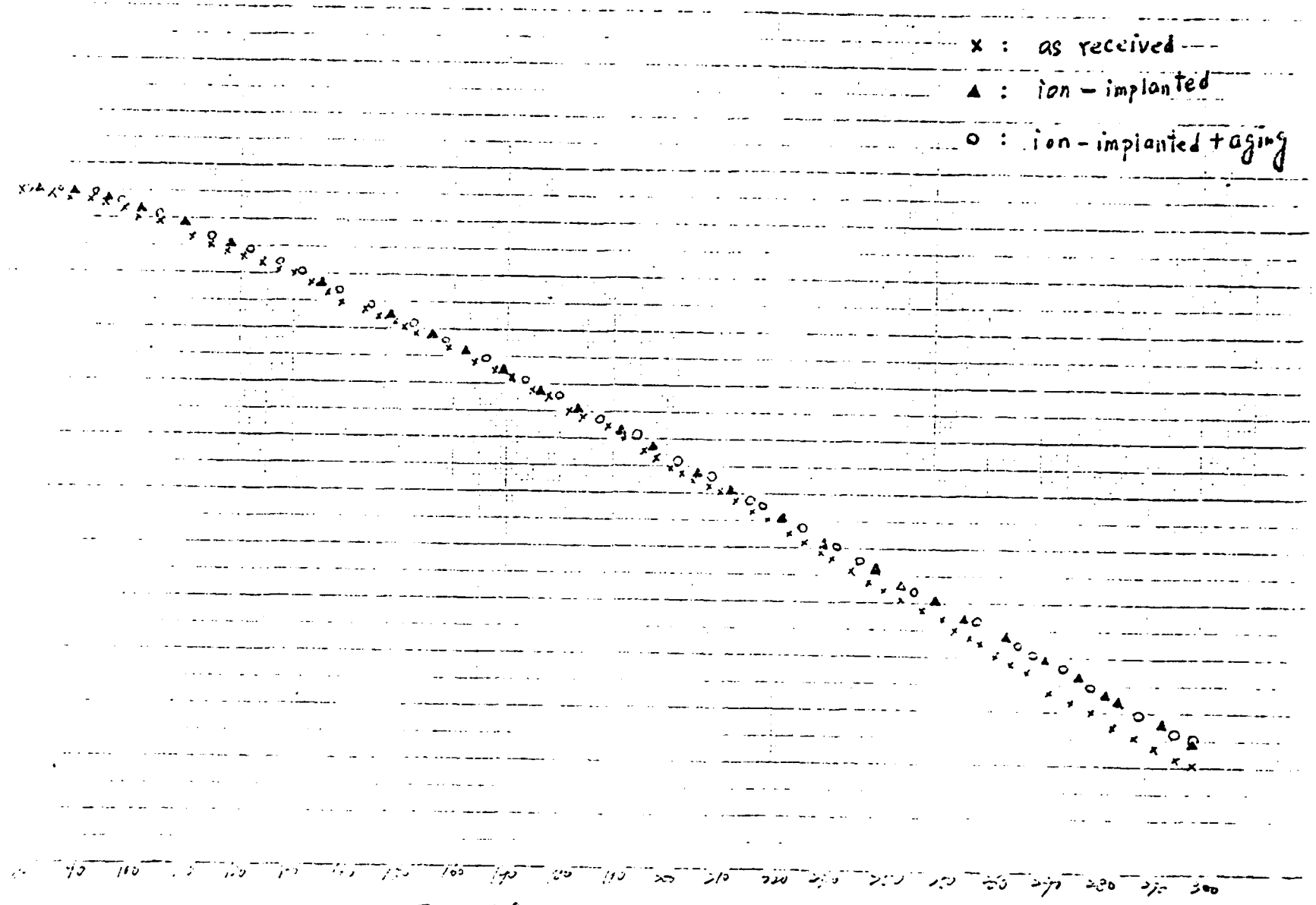

Fig 4

TRANSMISSION ELECTRON MICROSCOPIC STUDIES ON Be-IMPLANTED Cu AND As-IMPLANTED Au

Ion implantation has been used to modify the surface structure of metals (1, 2). A number of studies have been aimed at improving mechanical properties (eg., fatigue, wear, erosion) and chemical properties (eg., corrosion, catalysis) by ion implantation (3, 4).

Ion implantation involves a non-equilibrium method of superficial alloy formation, which in some cases has resulted in amorphous structures.

(a) Be-Cu System

The equilibrium phase diagram of the Be-Cu alloy system shows a eutectic reaction (5). Near the Cu-rich end the solubility of Be in Cu decreases with temperature. This is an ideal condition for the formation of age hardenable alloys. When a supersaturated solution of Be-Cu is quenched from the single-phase region (~550°C) and aged within the two-phase region, G.P. zones (6) can form, which can subsequently yield to equilibrium γ_2-phase precipitates. Since ion implantation has been shown to be similar to the ultrarapid quenching (7), it is reasonable to expect the formation of G.P. zones in Be-implanted Cu. However, in the present case the metastable G.P. zone was by-passed, and only the equilibrium γ_2 precipitate is observed to form. The reasons for this effect will be discussed below.

Be was implanted into Cu such that the near-surface region of the target material is of an alloy composition near the solidus curve. Be ions of 40 KeV energy were implanted to about 2.5×10^{16} Be/cm^2. The Cu foil was thermally connected to the sample holder in order to maintain the temperature of the

target material to a minimum. The temperature of the specimen was probably of the order of 100°C during implantation. Following implantation the material was ion-thinned a low current of 5 KV Ar. The thinned region was then observed in TEM.

The TEM results are shown in Figures 1a, b, c. Figure 1a shows a region which contains precipitates of the γ_2-phase. The size of the precipitate is approximately 100-200Å. The selected area diffraction pattern is shown in Figure 1b, where reflections are seen due to both the precipitate and the matrix. Reflection 1 in Figure 1b is due to the CuBe phase, which has a CsCl structure (ordered B.C.C structure). The hazy rings in the diffraction pattern are due to a thin layer highly microcrystalline alloy which results from radiation damage. Such experimental results of overlapping crystalline and amorphous diffraction patterns are not uncommon following implantation (1).

Figure 1c is the dark field micrograph imaged from a precipitate reflection, and depicts the distribution of the γ_2 second phase. The apparent absence of a coherent precipitate indicates that the implantation gave rise to sites for heterogeneous nucleation of an incoherent phase; i.e. γ_2. Coherent phases (eg., G.P. zones) generally form in perfect lattice, and copious radiation damage arising from Be implantation will preclude this. This effect is commonly observed in neutron irradiated age-hardening alloys, where equilibrium phases will be readily nucleated.

Implantation will thus result in both supersaturation and concomitant phase separation of a non-hardening second phase. Further work will be done to control this nucleation process and to thus prevent decomposition, and, thus, softening.

(b) As implanted into Au

There recently has been considerable research on implantation with metalloid atoms, eg., B^+, P^+, into transition metals (1, 7). In most of the cases of metalloid implantation, the resulting implanted layer is amorphous, particularly in those cases where the metal-metalloid combination is known to form a glass. The following is a study of As implanted into Au.

As of 1.8 MeV energy was implanted into Au, resulting in an areal concentration of 9×10^{16} As/cm^2. This corresponds to approximately 0.62 at % of As. The sample was then thinned as described above.

Figures 2a-f show the micrographs and selected area diffraction patterns of this implanted surface. Dark spots are seen in Fig. 2a which are believed due to radiation damage which occurred during ion thinning. Figure 2b is the SAD of the area in Figure 2a. The diffuse ring pattern indicates an amorphous surface. Heating was carried out on some of the implanted surfaces in the microscope. Figures 2c-e show the diffraction patterns for three different temperatures. It is observed that, with heating the material recrystallizes, the recrystallization temperature being below 550°C. The micrograph in Figure 2f shows spots which are believed to be As precipitates.

As has a very low equilibrium solubility in Au. Upon implantation, the large As atom will create disorder in the host lattice, giving rise to an amorphous structure.

Recent work by R. A. Kant et al (NRL, unpublished) has shown the crystalline nature of Sb-implanted Al. Here, Sb is a metalloid with a rhombohedral structure and Al is a metal with f.c.c. structure. Though the As-Au system is similar to the Sb-Al system, the former is amorphous whereas the latter is crystalline. We feel that the probable reason may be the low melting point of Al as compared to that of Au. The Al thus gives rise to higher diffusion

and faster recovery.

This present work is being expanded and extended to other systems.

(1) A. Ali, W. A. Grant and P. J. Grundy, Phil. Mag. B 37, 353, (1978).

(2) P. J. Grundy, Contemp. Phys. 18, 47 (1977).

(3) W. W. Hu, C. R. Clayton, H. Herman and J. K. Hirvonen, Script. Met. 12, (197ᵖ).

(4) Applications of Ion Beams to Metals, Ed. S. T. Picraux, E. P. EerNisse and F. L. Vook (Plenum, N.Y., 1974).

(5) A.S.M. Metals Handbook, Vol. 8.

(6) J. W. Martin, Precipitation Hardening, Pergamon Press, London (1968).

(7) P. V. Pavlov, E. I. Zorin, D. I. Tetelbaum et al, Phys. Stat. Sol. (a) 19, 373, (1973).

FIGURE CAPTIONS:

Fig. 1a Bright field micrograph of Be implanted Cu

Fig. 1b Electron Diffraction pattern for the above

Fig. 1c Dark field micrograph of CuBe precipitates

Fig. 2a Bright field micrograph of As implanted Au

Fig. 2b Electron Diffraction pattern at room temperature

Fig. 2c Electron Diffraction pattern at 460°C

Fig. 2d Electron Diffraction pattern at 555°C

Fig. 2e Electron Diffraction pattern at 790°C

Fig. 2f Bright field micrograph of As implanted Au at 790°C

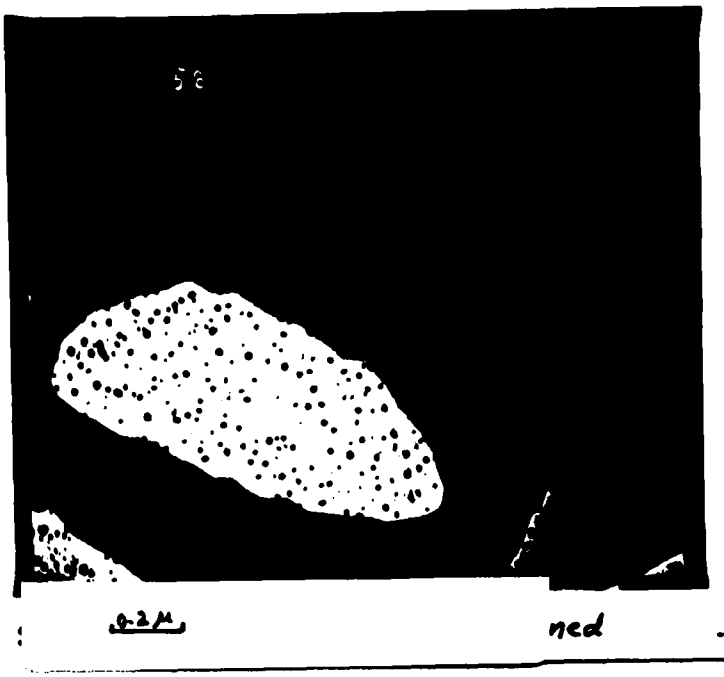

Fig. 1a

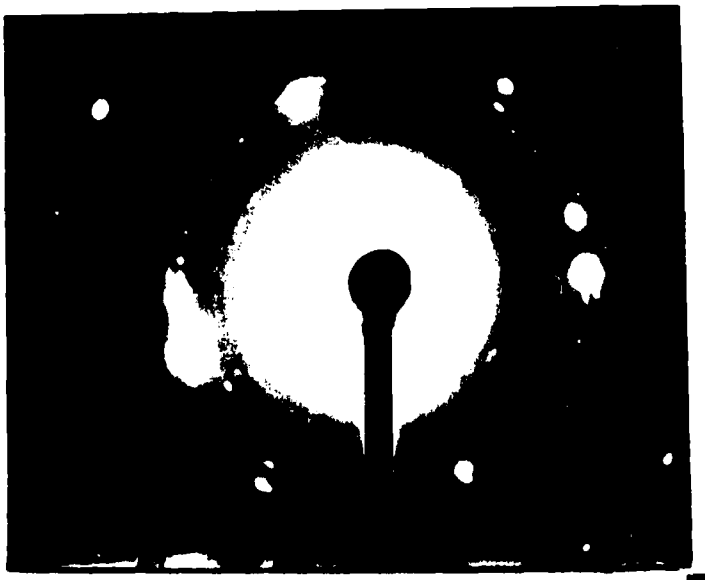

Fig. 1b

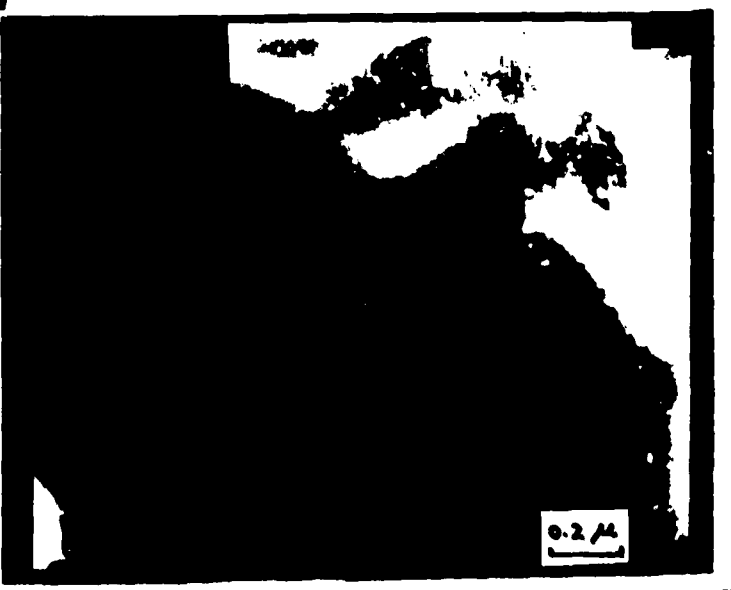

Fig. 1c

Fig. 2a

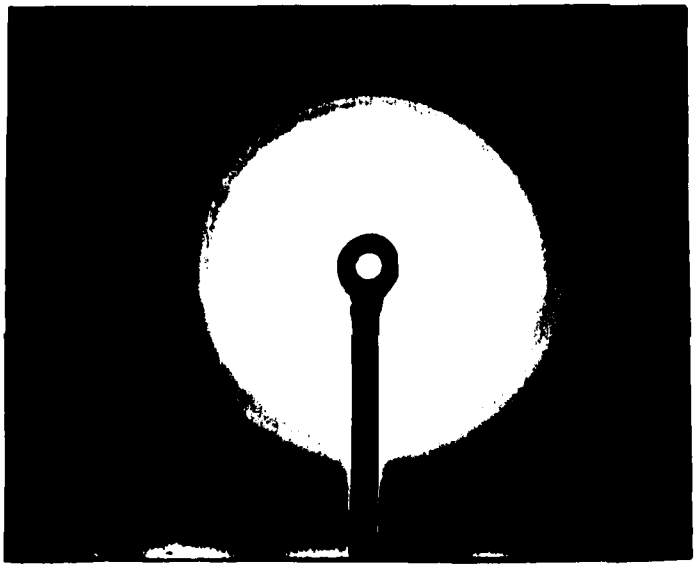

Fig. 2b

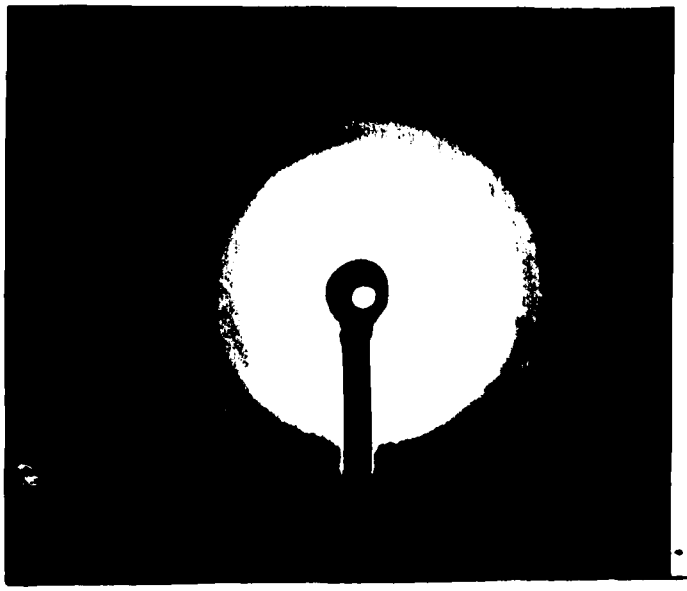

Fig. 2c
(460°C)

[460°C]

Fig. 2d
(555°C)

[555°C]

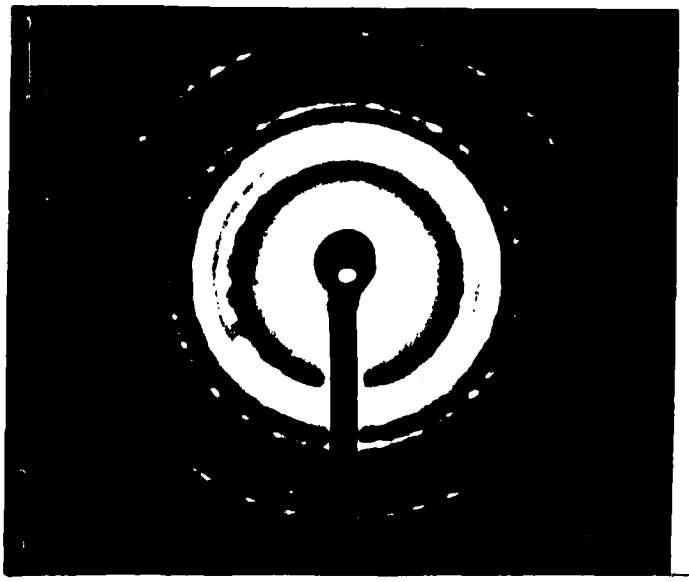

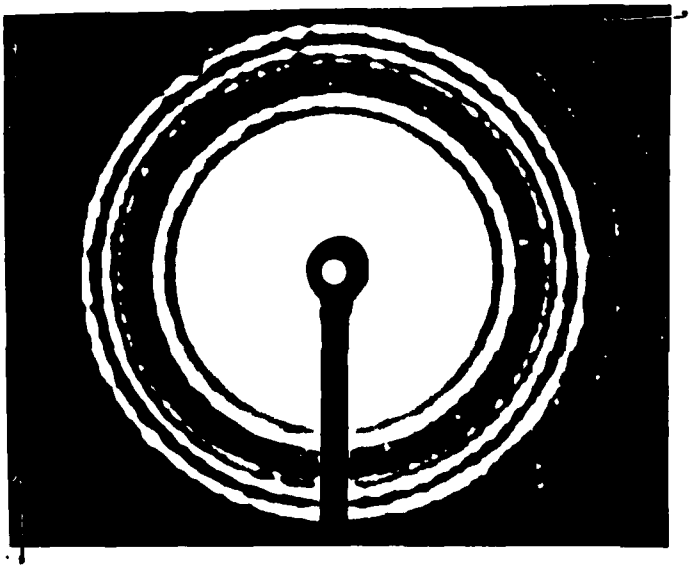

Fig. 2e
(790°C)

[790°C].

Fig. 2f
(790°C)

[790°C]

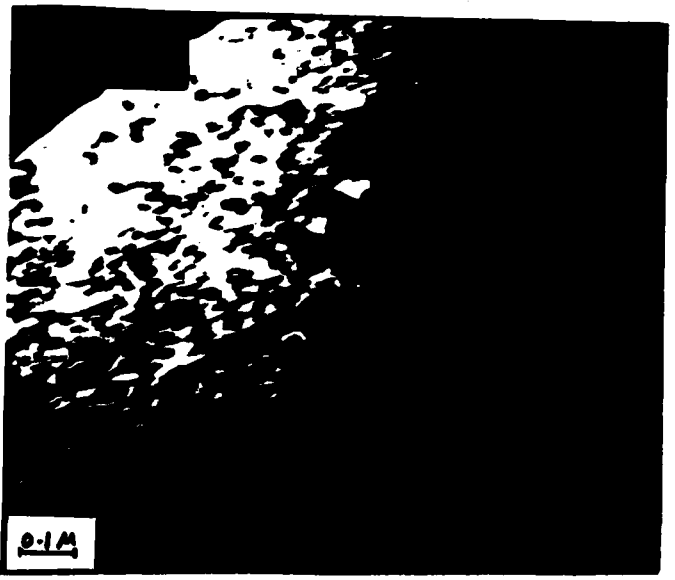


DATE
FILMED
2-8